remote sensing

MDPI

Article

From Polar Day to Polar Night: A Comprehensive Sun and Star Photometer Study of Trends in Arctic Aerosol Properties in Ny-Ålesund, Svalbard

Sandra Graßl [1,2,*], Christoph Ritter [1], Jonas Wilsch [3], Richard Herrmann [1,2], Lionel Doppler [4] and Roberto Román [5]

[1] Alfred-Wegener-Institut, Helmholtz-Zentrum für Polar- und Meeresforschung, Telegrafenberg A45, 14473 Potsdam, Germany
[2] Institut für Mathematik, Mathematisch-Naturwissenschaftliche Fakultät, Universität Potsdam, Am Neuen Palais 10, 14469 Potsdam, Germany
[3] Fakultät für Chemie, Georg-August-Universität, Tammannstraße 4, 37077 Göttingen, Germany
[4] Deutscher Wetterdienst, Meteorologisches Observatorium Lindenberg—Richard-Aßmann-Observatorium (DWD, MOL-RAO), Am Observatorium 12, 15848 Lindenberg, Germany
[5] Group of Atmospheric Optics (GOA-UVa), Universidad de Valladolid, Paseo Belén, 7, 47011 Valladolid, Spain
* Correspondence: sandra.grassl@awi.de

Abstract: The climate impact of Arctic aerosols, like the Arctic Haze, and their origin are not fully understood. Therefore, long-term aerosol observations in the Arctic are performed. In this study, we present a homogenised data set from a sun and star photometer operated in the European Arctic, in Ny-Ålesund, Svalbard, of the 20 years from 2004–2023. Due to polar day and polar night, it is crucial to use observations of both instruments. Their data is evaluated in the same way and follows the cloud-screening procedure of AERONET. Additionally, an improved method for the calibration of the star photometer is presented. We found out, that autumn and winter are generally more polluted and have larger particles than summer. While the monthly median Aerosol Optical Depth (AOD) decreases in spring, the AOD increases significantly in autumn. A clear signal of large particles during the Arctic Haze can not be distinguished from large aerosols in winter. With autocorrelation analysis, we found that AOD events usually occur with a duration of several hours. We also compared AOD events with large-scale processes, like large-scale oscillation patterns, sea ice, weather conditions, or wildfires in the Northern Hemisphere but did not find one single cause that clearly determines the Arctic AOD. Therefore the observed optical depth is a superposition of different aerosol sources.

Keywords: long-term AOD observations; aerosol optical depth (AOD); Ångström Exponent; seasonal trends; improvement of star photometer calibration; error estimation; polar aerosol; Arctic Haze; long-range aerosol transport

Citation: Graßl, S.; Ritter, C.; Wilsch, J.; Herrmann, R.; Doppler, L.; Román, R. From Polar Day to Polar Night: A Comprehensive Sun and Star Photometer Study of Trends in Arctic Aerosol Properties in Ny-Ålesund, Svalbard. *Remote Sens.* **2024**, *16*, 3725. https://doi.org/10.3390/rs16193725

Academic Editors: Jane Liu, Min Xie and Bingliang Zhuang

Received: 22 July 2024
Revised: 2 October 2024
Accepted: 3 October 2024
Published: 7 October 2024

1. Introduction

The so-called "Arctic Haze" was first observed by pilots in the 1950s, primarily occurring from March to May [1]. Photometer studies revealed particles up to a size of 0.2 µm with increased sulfate concentrations like [2,3]. Extensive airborne research investigated the origin and properties of the Arctic Haze in the 1980s like [1–3]. The particles strongly scatter but weakly absorb light, which reduces the overall visibility. The haze is mainly found in the lower 5 km of the troposphere and is vertically as well as spatially highly heterogeneously distributed [4,5]. Due to the general high surface albedo and enhanced multiple scattering in the Arctic, aerosol-radiative interactions are additionally increased within the haze layer [6,7].

The Arctic, especially in the European sector around Svalbard, undergoes a drastic temperature increase. This is most pronounced during winter with up to 3 K per decade [8].

From year to year, more and more sea ice retreats, which enhances the warming furthermore and contributes to "Arctic Amplification". The retreating sea ice enhances the role of the open sea, which is a local aerosol source (like sea salt) and is also a sink for long-range transported aerosols in the Arctic [9]. Atmospheric aerosols play a crucial role in the climate through direct and indirect interactions, for example, with respect to solar radiation or clouds [10]. Due to their various appearances in size, shape or chemical composition, they can interact differently with solar radiation, leading to either a surface warming or cooling. Therefore, radiative forcing is still the most uncertain aspect in climate models [11–13]. Due to the high spatial and temporal variability of aerosol occurrences and concentrations, long-term observations are important to understand climate changes. Several studies like [14] have found changes in aerosol types throughout the last decades. While anthropogenic emissions are globally reduced [14], a clear annual cycle can still be found in all parts of the Arctic. Concentrations of ultrafine particles have increased, which is linked to changes in airmass transport regimes and increased transportation time over open water [15].

The monitoring of aerosol load and properties is especially interesting in the Arctic, since it is nearly free of anthropogenic sources [6]. Several ground-based and automatically measuring instruments, like photometers, are set up there to gain long-term time series of atmospheric conditions. Photometers retrieve the integrated extinction, Aerosol Optical Depth (AOD), of the entire atmospheric column by measuring the intensity of extraterrestrial light sources, like the stars, Moon and Sun. Sites with exceptionally long-term data series are for example Barrow (USA), Alert (Canada) in the American and Ny-Ålesund, Svalbard, in the European Arctic.

Since the Arctic generally has fewer aerosol sources than the midlatitudes and the warming takes place strongest globally, it is a very important observation site and many different studies have been performed already to investigate changes in the aerosol budget with various passive and active remote sensing instruments as well as in situ observations, for example [16–18]. It is also seen in Figure 1 that different processes interact with aerosols in the Arctic and depend on the time of the year as well. In our study, we try to provide a comprehensive picture of changes in Arctic aerosols due to several processes. We will take local marine aerosol, sea spray primary aerosol, sea ice cover and precipitation into account. For the investigation, we homogenised sun and star photometer data sets for the years 2004–2023 and analyse aerosol load and properties for every month measured in Ny-Ålesund, Svalbard. The aim of this study is to analyse changes of aerosol properties within 20 years of continuous observation.

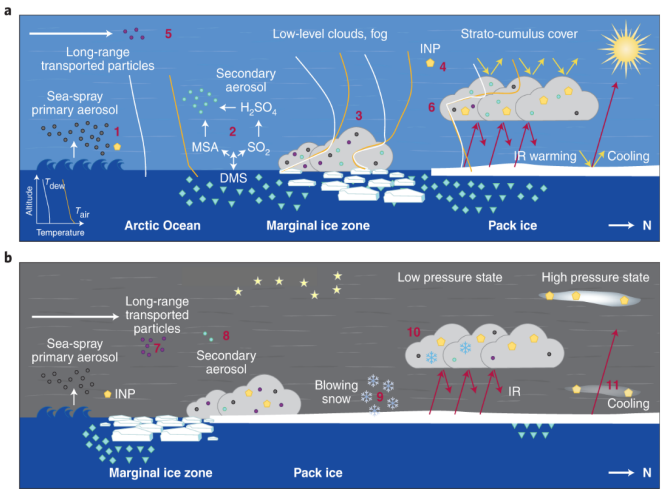

Figure 1. Different relevant processes during polar day (**a**) and polar night (**b**). The numbers indicate (1) sea spray formation; (2a–b and 8) (non-)marine secondary aerosol formation; (3) particle processing in fog; (4) Arctic Ice Nucleation Particles (INP) concentrations; (5 and 7) Long-range transport; (6, 10 and 11) cloud formation; (9) blowing snow. Figure is adapted from Schmale et al. [14].

2. Measurement Site and Instruments

Sun and star photometers are located at the meteorological observatory of AWIPEV, the German-French Arctic research station, in Ny-Ålesund, an international super-site for environmental research in the European Arctic. Ny-Ålesund is located at 78.9°N 11.9°E.

Since Ny-Ålesund is located beyond the Arctic circle, polar day and night strongly affect photometer measurements. Polar day starts on 17 April and lasts until 26 August. Limitations for Sun observations by photometer also occur due to the mountain ridge in the South (Figure 2). A large data gap is usually in October and November, when the elevation of the Sun is low or even beneath the horizon, but the cloud fraction is also very high and star photometer measurements are therefore not possible [19]. In February, the Sun is already above the horizon. But because of the orography, the first sun photometer measurements occurs only on 8 March. For the other part of the year (November to beginning of March), the star photometer is the only instrument used for photometer measurements. Therefore, it is important to combine and homogenise both data sets to see the changes in aerosol optical depth throughout an entire year. Lunar photometer measurements are just available for half a Moon cycle and are also only suitable for observations during polar night, but not included in this study.

The sun photometer, used in this study, was manufactured by Dr. Schulz & Partner GmbH (Rietz-Neuendorf, Germany). It has a temporal resolution of 1 min and measures the incoming direct solar radiation with a photo diode. The total optical depth is calculated following Lambert-Beer law and guidelines by WMO [20]. The sun photometer had 17 filters for wavelengths from 355.4 nm to 1089.0 nm until 2012. After 2012, only 10 of these 17 filters have been kept, and the spectral range is now reduced to 369 nm to 1022.9 nm. This instrument is regularly calibrated at Observatory Izaña, Tenerife, Spain, using the Langley Plot method. More information about the instrument is given by Graßl and Ritter [9], Stock [21]. The raw data can be found at the data repository PANGAEA [22].

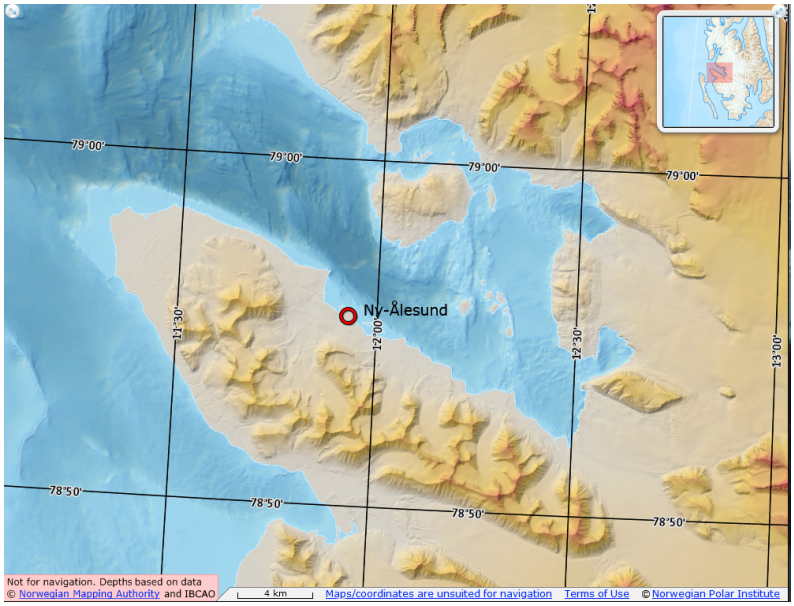

Figure 2. Map of Ny-Ålesund on Svalbard in the European Arctic (source: Svalbardkartet (https://geokart.npolar.no/Html5Viewer/index.html?viewer=Svalbardkartet, accessed on 2 October 2024)); courtesy of Norwegian Polar Institute.

The star photometer was also manufactured by Dr. Schulz & Partner GmbH. It measures the spectral intensity of various stars. The operator chooses the stars before each measurement cycle. The instrument collects the light via a Celestron C11 Telescope (aperture length of 280 mm, focal length of 2800 mm) and guides the light further to a CCD.

To find the star and perform the fine adjustment of the altazimuth mount, two different cameras are needed. They have a viewing angle of 53 arcmin and 9 arcmin, respectively. A grating spectrometer is connected behind the telescope. Our instrument combines ten measurement signals into one raw signal to increase the overall signal-to-noise-ratio.

After the star is manually selected, the tracking of the star is performed automatically. The filter wheel of the star photometer had 10 filters from 381.6 nm to 1037.7 nm until it was modified in 2010. Afterwards, a second filter wheel was included, which changed the measurement range from 420.0 nm to 1040.6 nm and increased the number of filters to 17. More information about the instrument can be found at Herber et al. [16], Graßl [23]. The raw star photometer data is available at the data repository PANGAEA [24].

Usually the star photometer performs standard measurement by observing one star, which is very similar to lunar or Sun photometry. Both measurement techniques are explained in greater detail by Graßl [23]. In Ny-Ålesund, we only use the four stars Vega (α Lyr), Altair (α Aql), Merak (β UMa) and Alhena (γ Gem). A more detailed description of the measurement principle of the star photometer can be found in Section 3 and an analysis of the sensitivity towards measurement errors is presented in Appendix A.

3. New Method for Star Photometer

The general observation via star photometer is a so-called "One Star Measurement" (OSM). The photometer points towards the selected star and measures its apparent intensity with every filter. The temporal resolution is set to 5 min, which is also determined by the time the mount needs to switch between pointing to the star and the background as well as the integration time during the observation of the star. Since all stars are by far not as bright as the Sun, the integration time needs to be increased compared to sun photometers. To calibrate the star photometer every season, a Two Star Measurement (TSM) needs to be performed by a suitable pair of stars. This require several perfect nights. A perfect night is a cloud free and homogeneous and stable atmospheric conditions. With the built-in software of our instrument, these calibration files need to be created manually, an automatisation of this procedure is not possible. A TSM has a temporal resolution of about 10 min due to the scanning of two stars.

We improve this process. The new procedure requires only one perfect night per winter during which we perform the TSM. We take for each star of the TSM the calibration values, and can apply them to the standard OSM process of AOD monitoring. These calibration values are valuable for a duration of about one year:

By using Lambert–Beer Law the extraterrestrial intensity, RS_0^1, can be calculated. In the following, the reference star will be star 1. The two stars have a difference in apparent stellar magnitudes, Δmag. Hence, the unknown extraterrestrial intensity of star 2 can be calculated:

$$RS_0^2 = RS_0^1 \cdot 10^{-0.4 \cdot \Delta mag} \tag{1}$$

The total optical depth, $\tau_{tot}(\lambda)$, follows, using Bear–Lambert and Equation (1):

$$\tau_{tot}(\lambda) = -\frac{1}{m_{tot}} \cdot \ln\left(\frac{RS_{meas}^2(\lambda)}{RS_0^2(\lambda)}\right) = -\frac{1}{m_{tot}} \cdot \ln\left(\frac{RS_{meas}^2(\lambda)}{RS_0^1(\lambda) \cdot 10^{-0.4 \cdot \Delta mag}}\right) \tag{2}$$

These steps have to be performed for every wavelength of every star accordingly. As external information, only the wavelength-dependent apparent magnitudes of different stars needs to be looked up from astronomical websites, like Stellarium (https://stellarium-web.org/, accessed on 3 October 2024) , and one TSM calibration in good conditions per season needs to be done to keep the error in the calculation of the total optical depth as small as possible. TSM calibration in good conditions means: completely cloud free and homogeneous and stable atmospheric conditions during a long time, and small difference in azimuth angles for each pair of stars used for the TSM.

4. Data Processing of Star and Sun Photometer

The total optical depth, τ_{tot}, is calculated using either the measured voltage of the sun photometer or photo counts via the star photometer. Several corrections are applied to obtain the AOD, τ_{aer}:

$$\begin{aligned} \tau_{tot} m_{tot} &= \tau_{aer} m_{aer} + \tau_{Ray} m_{Ray} + \tau_{O_3} m_{O_3} \\ \tau_{aer} &= \frac{1}{m_{aer}} \left[\tau_{tot} m_{tot} - \tau_{Ray} m_{Ray} - \tau_{O_3} m_{O_3} \right] \end{aligned} \tag{3}$$

with the terms for optical depth τ and airmass m for the aerosol contribution indicated by *aer* for aerosol or *Ray* for Rayleigh scattering and O_3 for Ozone absorption. For simplicity, τ_{aer} at $\lambda = 500$ nm is stated as τ, if not stated otherwise.

4.1. Ozone Correction

Daily averages of ozone ECMWF-reanalysis data of CAMSRA (Copernicus Atmosphere Monitoring Service reanalysis of the atmospheric composition) [25] are used for the calculation of the ozone optical depth for both instruments, since this data set is available as well for polar day and for polar night. It provides a 3-hourly analysis for several greenhouse gases, ozone and aerosols at a spatial resolution of $0.75° \times 0.75°$. For this analysis, we used data from January 2003 onwards, which is the beginning of the dataset.

4.2. Cloud Screening

To remove cloud-contaminated data from the data sets, cloud screening is applied according to AERONET standards [26] with some modification due to slight differences between the instruments used at AERONET and AWIPEV. Only measurement points that fulfil all these criteria are considered as cloud-free and used for further analysis:

- If $\tau(\lambda) < -0.01$, the measurement point is rejected for this wavelength;
- A measurement triplet consists of three measurement points for a single wavelength. For the sun photometer, this is equivalent to 3 min, for the star photometer, a triplet has a duration of 15 min due to its coarser time resolution. The variability between maximum and minimum of the triplet shall be smaller than 0.02;
- If the standard deviation of daily averaged $\tau \leq 0.015$, the cloud-screening process is stopped;
- If the Ångström Exponent is smaller than three times standard deviation around the daily mean AE, the cloud-screening process is stopped;
- The smoothness criterion of the time series is based on limiting the root mean square of the AOD second derivative with time. The second derivative is very sensitive to local oscillations of the cloud optical depth and the threshold of $D \leq 16$ between two adjacent measurement points is applied closely following Smirnov et al. [26]. The value for the threshold is determined analytically and based on measurement data;
- Measurements with $\tau \geq 1$ are flagged as clouds. This criterion might eliminate some aerosol measurements but due to the remoteness of the location, these cases are rare;
- For sun photometer only: A lower threshold for the measured voltage is set to 10 V;
- If the remaining cloud-free time of measurements is less than 20 min, we discard the entire day in order to have a representative measurement time of the day.

4.3. Data Availability

Throughout the year, the data coverage is very variable. A big annual and inter-annual variability can be found. The relative availability of measurement points per year is given in Figure 3 for both instruments separately. It is the combination of the star and sun photometer.

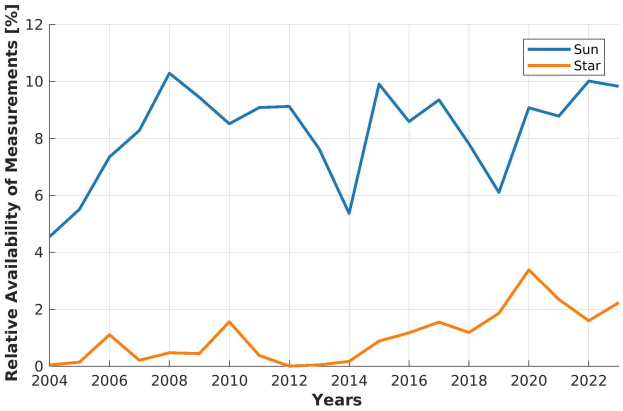

Figure 3. Relative availability of cloud-screened measurements [%] over the course of a year separated between sun and star photometer.

From November to February only star photometer observations are available. September, October and March are covered by both instruments. The big deviation between sun and star photometers has two main reasons: While the sun photometer measures automatically, the star photometer has to be operated manually, often also during night times, when the standard operator on site is not available. The second reason is the operating limitations of the star photometers. The Sun has to be at least 8° below the horizon in order for the sky to be dark enough for measurements using the stars, while the sun photometer requires a solar elevation of a minimum of 5°. The reduction in measurement time in 2012 can be explained by purely two star measurements, because the temporal resolution of it is 10 min and hence twice as long as a one star measurement. The number of measurement days after cloud-screening is given in Table 1. Since it is difficult to detect thin clouds manually or even with the help of thermal cameras during darkness and a cold atmosphere, lots of star photometer measurements have been operated in cloudy conditions, and have been excluded of the dataset during the cloud screening procedure explained in Section 4.2.

Table 1. Numbers of measurement days per month and year after cloud-screening for sun and star photometers individually. The star photometer measurement is noted in $(\cdot)$. In the time of the year in which only one instrument is operational, the other instrument is not reported in the table.

	Jan	Feb	Mar	Apr	May	June	Jul	Aug	Sep	Oct	Nov	Dec
2004	(8)	(10)	(0) 8	11	24	24	26	24	23	(0) 2	(0)	(0)
2005	(3)	(9)	(0) 3	14	23	10	11	11	9	(0) 0	(0)	(0)
2006	(2)	(15)	(20) 14	27	27	24	22	18	22	(0) 2	(0)	(9)
2007	(11)	(4)	(8) 20	23	18	23	26	20	18	(2) 0	(3)	(6)
2008	(11)	(1)	(5) 23	28	21	26	24	25	17	(8) 2	(6)	(7)
2009	(8)	(8)	(7) 16	23	21	17	24	17	20	(0) 0	(6)	(4)
2010	(5)	(18)	(13) 19	26	18	23	25	23	18	(0) 0	(13)	(12)
2011	(15)	(9)	(0) 7	22	20	22	21	18	0	(0) 0	(4)	(3)
2012	(1)	(1)	(1) 9	28	28	25	26	21	15	(0) 3	(4)	(0)
2013	(0)	(3)	(0) 9	26	17	14	20	21	19	(8) 1	(5)	(3)
2014	(5)	(0)	(8) 10	11	7	18	18	27	9	(0) 0	(0)	(0)
2015	(6)	(4)	(5) 8	28	25	23	25	25	22	(4) 1	(12)	(8)
2016	(10)	(11)	(15) 16	24	21	16	19	26	18	(0) 1	(9)	(6)
2017	(13)	(4)	(6) 8	28	26	20	22	17	12	(1) 3	(18)	(12)
2018	(9)	(9)	(11) 19	24	22	16	19	26	21	(0) 3	(0)	(0)
2019	(11)	(9)	(2) 10	17	22	25	3	10	23	(0) 1	(11)	(9)
2020	(11)	(19)	(13) 4	25	26	24	26	25	12	(10) 1	(7)	(8)
2021	(15)	(2)	(0) 12	29	26	24	23	22	18	(4) 1	(14)	(9)
2022	(4)	(14)	(2) 13	29	28	21	21	19	11	(10) 0	(8)	(16)
2023	(8)	(3)	(10) 16	15	23	25	25	19	16	(9) 0	(15)	(7)

5. Results

The treatment of raw data as well as cloud-screening was performed in the same way for both instruments. Afterwards, the two datasets of each instrument are merged in one homogeneous common "day&night" dataset. The AOD measurements are only available during cloud free time. Hence, there is also a clear-sky bias in the data evaluation. High aerosol events, which arrived during cloudy/rainy conditions, can therefore not be captured by photometer observations. Data of some months will be neglected due to the small number of measurement time, since a daily median is only calculated, if the measurement was at least 60 min long and the criterion of Section 4.2 is extendet. A monthly median is only taken into account, if at least 5 daily median values exist. This criterion is much stricter than in other studies like [27,28] to obtain a more representative data set.

5.1. Overview of the Data

The available data is presented in Figure 4, where each point is the daily median AOD. The daily AOD is generally low and the star photometer fills the gaps of polar night. We notice a large variability from year to year, especially for the star photometer data set (green points). This picture demonstrates the complementary nature of the two instrument datasets (sun and star photometers): One instrument fills the gaps without data of the other one. Moreover, since the gaps are very long (four months polar day or night), Figure 4 demonstrates, how important it is, to have in polar regions as well an instrument operating during the night (star photometer) as operating during the day (sun photometer).

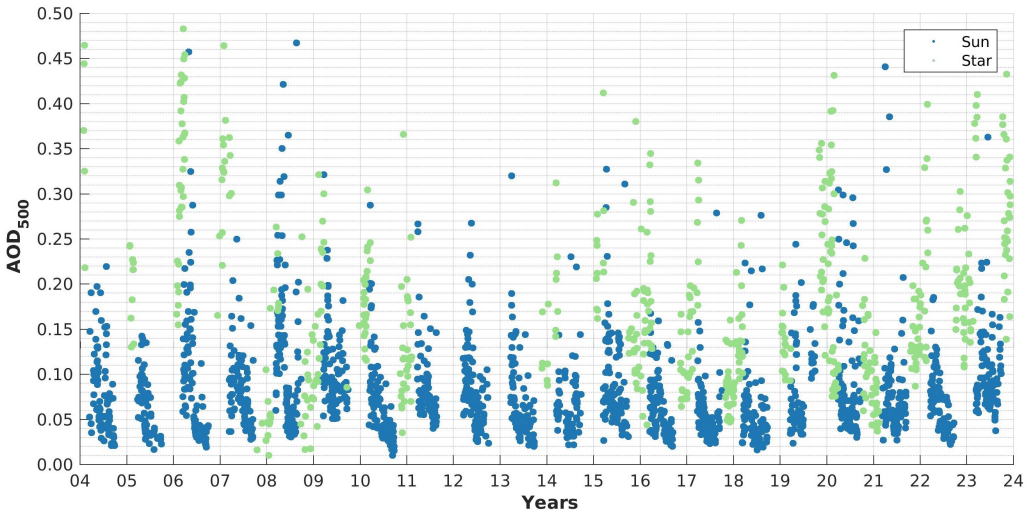

Figure 4. Overview of combined photometer data. Every point is a daily median AOD.

5.2. Monthly Changes of AOD

Figure 5 gives an overview of monthly median AOD observations over the entire measurement period 2004–2023. A detailed distribution for every month and year is provided in Figure 6.

Winter (October to March), appears with heterogeneous monthly median AOD observations. The difference in median AOD between summer and winter exceeds 0.1 and the median AOD in winter is on average three times higher than in summer. During the time of the Arctic Haze in early spring (March and April), mean monthly median AOD is about 0.04 higher than during the summer (June to September). While these months show a low year-to-year variability, April and May show a broader variability, indicating less stable atmospheric conditions and an influence of different aerosol events occurring in Ny-Ålesund.

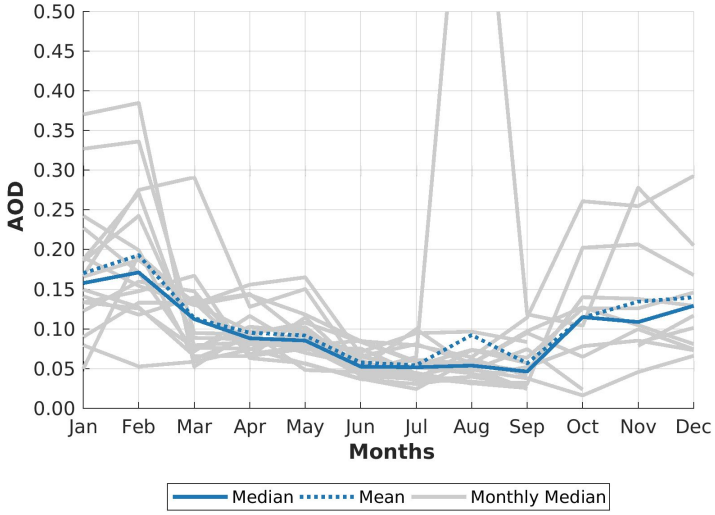

Figure 5. The monthly median values for the AOD is shown for each year of 2004–2023 in grey. The blue lines indicate the median (solid) and mean (dashed) of these values.

The months from March to September are generally characterised by a small variability between the years and a low AOD with small variability within a month. Some months and years with exceptional high AOD can still be found, but they indicate a single individual event, rather than a general trend. The exceptional high AOD in August 2019, which is already described in much detail by Xian et al. [29].

Winters (October to February) have a pronounced increase in AOD, particularly in January, which is characterised by an elevated AOD in general and a high variability of it. The tendency shows that this season is increasingly polluted over the last two decades, with a year-to-year variability being more significant compared to summer. In the recent years, a noticeable increase in AOD was found from October to February, indicating that a change of aerosol load and/or properties has happened. The number of measurement days in October and November is sparse (see Table 1), which is partially caused by an enhancement of arriving storms compared to other seasons by increasing the cloud cover. Even though the observational time is reduced in winter compared to summer. Our dataset reveals this enhancement of the AOD.

During the time of the Arctic Haze (March and April) the AOD is significantly reduced compared to winter, but is much higher than during summer.

Median AOD in summer (May to September) is in general lower than in winter, with less variability between adjacent years, with a yearly minimum in August. However, an extraordinary spike in AOD was observed in mid-July to early August 2019 due to wildfires and transported aerosols. This was not captured in our July data due to maintenance issues and is further discussed by Xian et al. [29]. We did not observe a general increasing monthly AOD in the recent years (2004–2023). The difference is relatively small in summer, but large in winter. Due to many storms in autumn, the cloud cover is high (up to 80%) [19], see Table 1.

As a summary of the results' analysis: Winter (October to February) is a highly polluted time of the year, what is surprising for the pristine environment of the Arctic. The importance of the Arctic Haze is clearly being reduced, since winter is the most polluted season, while simultaneously the amplitude between minimum and maximum of the median becomes larger and larger over the available measurement time. Several different reasons for this change will be discussed in the Sections 5.3 and 5.7.

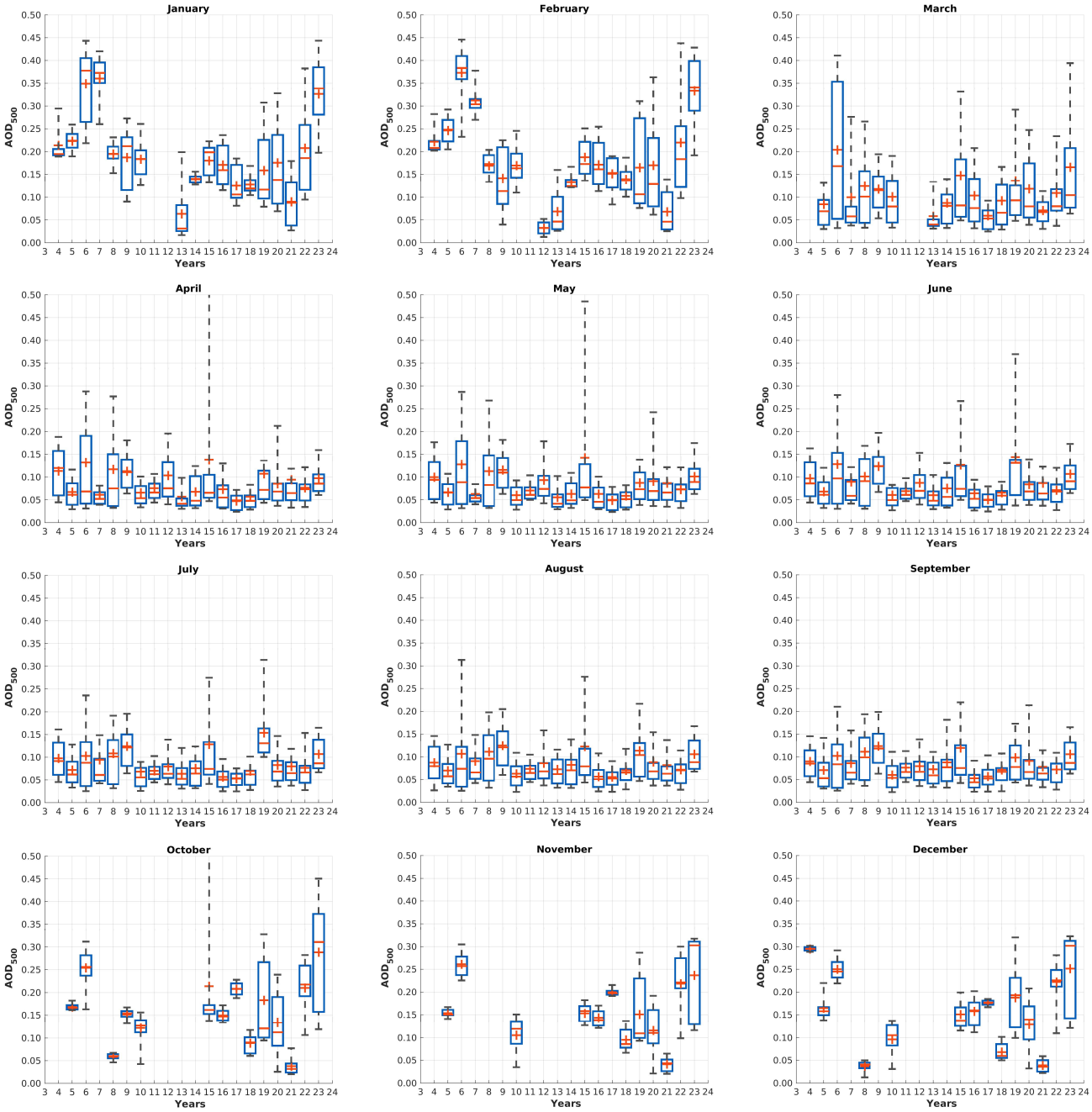

Figure 6. Box-and-whisker plots for AOD for every month measured by sun and star photometer. All individual data points after cloud-screening are taken into account. As a reference for the amount of data per month and year, see Table 1. 25th and 75th percentile are shown by the blue boxes, whiskers indicated 9th and 91th percentile, median is shown by − and mean by +.

5.3. Trend Analysis for AOD

As already shown in Figure 6, the AOD varies between years and months significantly. In the following, linear trends of the Arctic AOD are analysed by month (Figure 7).

For a more substantial analysis of changes in AOD, a trend analysis is performed, first for the entire period of 2004–2023, afterwards for every decade separately. The results of the linear trend for each month and the corresponding standard deviation for this month are presented in Table 2. The trend is calculated over the entire observation period and has the unit $\left[\frac{1}{20\ yr}\right]$. The 2σ interval is used to determine the uncertainty of the trend analysis.

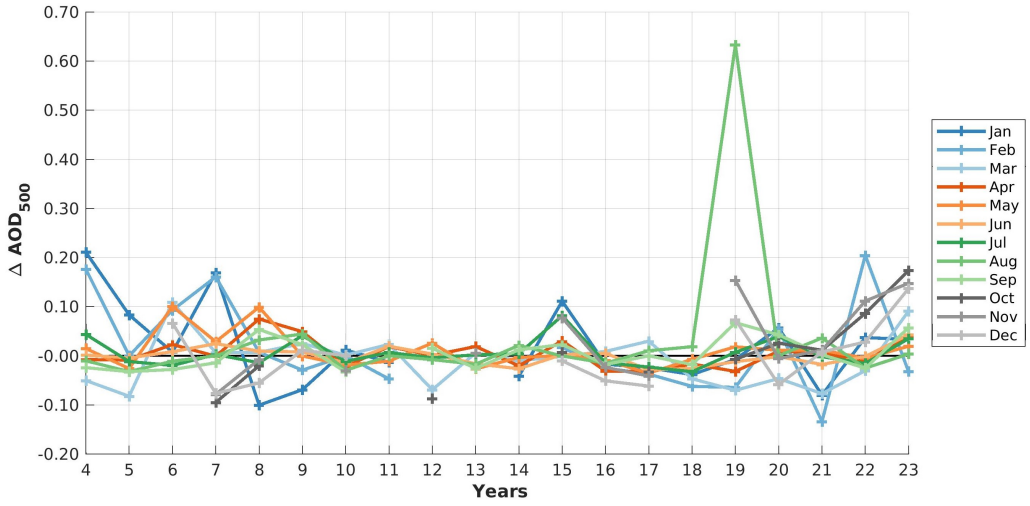

Figure 7. Deviation from monthly mean AOD values in dependency of the year.

Table 2. The monthly linear trend of monthly median AOD in $\left[\frac{1}{20\ yr}\right]$ and its standard deviation of the monthly median of τ for the years 2004–2023 with combined sun and star photometers. The 2σ interval gives the uncertainty range.

	Jan	Feb	Mar	Apr	May	Jun	Jul	Aug	Sep	Oct	Nov	Dec
Trend $[\times 10^{-3}]$	−4.30	−4.91	−0.82	−0.10	−1.67	−0.46	0.12	5.82	2.15	10.72	9.30	3.34
Std	0.08	0.09	0.05	0.03	0.04	0.02	0.03	0.14	0.03	0.08	0.08	0.06
2σ interval	0.15	0.17	0.12	0.06	0.06	0.04	0.06	0.27	0.06	0.11	0.10	0.13

Over the entire observation time (2004–2023), the months April to June and especially May became clearer with a reduction in up to $\Delta\tau = -1.7 \times 10^{-3} \frac{1}{20\ yr}$, while the AOD in October and November increased with up to $\Delta\tau = 10.1 \times 10^{-3} \frac{1}{20\ yr}$. In agreement with Figure 5, the standard deviation is larger for winter and smaller for summer with values around 0.02 (June), indicating that the monthly median AOD in summer changed less from year to year than in winter (0.09 in February). A significant decrease in AOD can be found in January and February. When also taking Figure 6 into account, it can be seen, that this trend happened until the year 2020. Afterwards, a constant increasing of AOD is observed. Therefore, this linear trend only reflects roughly real changes. Generally, it can be seen that autumn becomes more polluted, while a small decrease in AOD can be found during spring.

We also tried to investigate the trend over one decade (2004–2013 and 2014–2023, respectively), but the large variability between two consecutive years of the same month does not allow a trend analysis. Hence, we stick to a twenty year long trend analysis.

5.4. Case Study: Polar Stratospheric Clouds

Polar Stratospheric Clouds (PSC) can occur in the Arctic lower stratosphere, when the temperature drops below 195 K. PSCs provide the surface, on which chemical reaction can take place to form free chlorine radicals, which directly destroy ozone molecules. Due to the required low temperatures of the atmosphere, they are typically observed in Ny-Ålesund between December and February [30]. While the global temperature in the troposphere increases significantly due to climate change, the stratosphere cools down at the same time [31]. This effect enhances the probability of PSC formation. Therefore, it is not trivial to directly transfer older studies like [32,33] to today's occurrence probabilities of PSCs. Since these stratospheric clouds occur above Ny-Ålesund only during winter, when in parallel the AOD is significantly higher than during summer time, we estimate the possible impact of a PSC to star photometer observations. To obtain a height-dependent information about the PSC, we use additional Raman Lidar data. By measuring the back-scattering

coefficient of aerosol and cloud layers, distinct and different layers can be identified. The presented ground-based observations (Figure 8) by the Raman Lidar KARL (Koldewey Aerosol Raman Lidar), which is operated manually from Ny-Ålesund, shows one exemplary day with a thick and persistent PSC in February 2020. The temporal resolution is 10 min with a spatial resolution of 60 m. More information about the Raman Lidar KARL can be found at Hoffmann [34]. A rough estimation of the AOD can be obtained from the extinction coefficient measured of a Raman Lidar. More information about the calculation of the AOD are described by Herrmann et al. [35].

Figure 8 shows an example of a PSC in around 17 km to 20 km on 9 February 2020. As Massoli et al. [33] showed, the temperature in the lower stratosphere can change rapidly from day to day, which immediately can stop the formation of PSCs or shift it into higher/lower altitudes. Generally, it can be seen in Figure 8 the lower troposphere is quite polluted, indicated by high back-scatter values. This also supports the observations by the star photometer, which generally see a high aerosol load during the entire winter (see Figure 6) with comparably large particles (later discussed in Section 5.5).

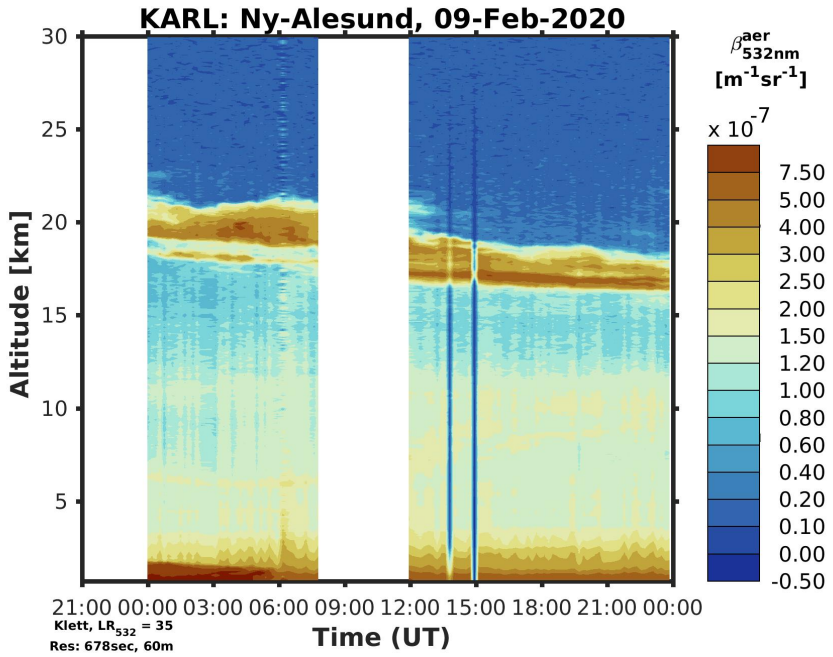

Figure 8. One exemplary day with PSC (9 February 2020), measured by the Raman Lidar KARL in Ny-Ålesund. The PSC is clearly visible in about 20 km altitude throughout the entire day.

Regularisation methods are used to retrieve the optical depth of this PSC. An optical depth of the PSC by Lidar is estimated to $\tau_{532}^{PSC} = 0.06$ for the time period 5:09 UT to 6:40 UT. Parallel star photometer measurements with the star Merak reveal a mean aerosol optical depth for the entire atmospheric column of $\tau_{532}^{Ph} = 0.11$. Merak had during this measurement an elevation between $62°43'$ and $58°31'$. The Sun moved during this measurement from an elevation of about $-18°$ to $-13°$.

The above described PSC dominates the back-scatter coefficient of the low stratosphere, but its contribution to the AOD measured by the star photometer is only an offset of $\Delta\tau = 0.06$. Even if we correct the complete winter AOD dataset from this $\Delta\tau = 0.06$ PSC offset, supposing a PSC cover of 100 %, the winter months would still have higher AOD values than the summer months (see Figure 5). As Maturilli et al. [32] have shown, polar stratospheric clouds do not occur constantly in the Arctic winter stratosphere. Hence, the enhancement of AOD in winter cannot be caused by PSC-contamination in star photometer data, but is rather caused by aerosol layers.

5.5. Ångström Exponent

The Ångström Exponent is a very important parameter to determine the effective size of aerosols. The evaluation of the Ångström Exponent is only performed for cloud-screened data. It is defined according to Ångström [36] as followed:

$$AE = -\frac{\partial \ln \tau_{aer}(\lambda)}{\partial \ln \lambda} \rightarrow \begin{cases} 4 & \text{, small particles, Rayleigh scattering} \\ 0 & \text{, large particles, grey scattering} \end{cases} \quad (4)$$

In this work, AE has been calculated as a linear fit of $ln(\tau)$ and $-ln(\lambda)$ considering at least six wavelengths in the range between 413 nm and 862 nm (before 2013) and 381 nm to 779 nm (after 2013) for the sun photometer. For the star photometer, the Ångström Exponent is calculated with seven wavelengths between 381 nm and 861 nm (before 2006), with eight wavelengths until 2010 (413 nm to 861 nm) and from 2010 onwards between 450 nm and 862 nm with ten wavelengths.

Similar to Figure 4 (for AOD), Figure 9 shows the daily median Ångström Exponent for both instruments from 2004–2023. As can be seen, most of the AE values concentrate within the range of $AE \in [0, 1.8]$. Some exceptions are recorded for values $AE > 2$.

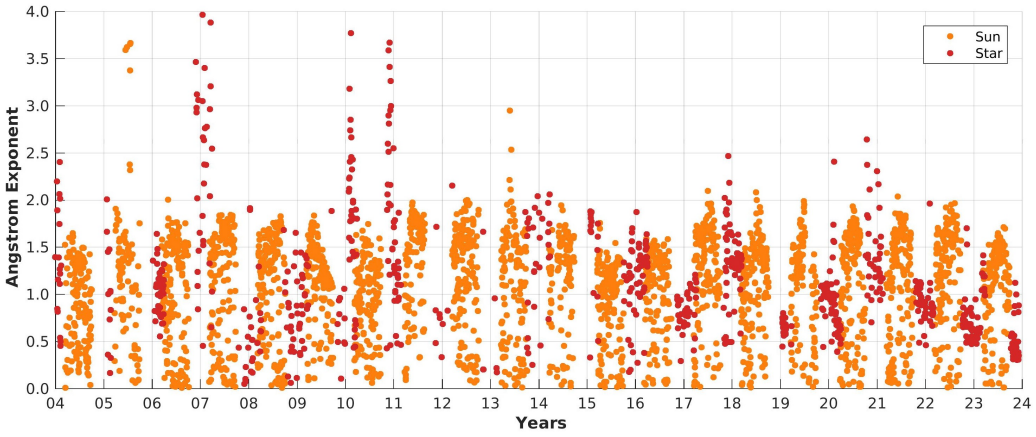

Figure 9. Daily median of Ångström Exponent for sun and star photometer.

Figure 10 gives a relative overview about the density of AOD versus AE, where yellow indicates a high density of combination and blue colors a low one for the two photometer data sets separately for a resolution of 1 min.

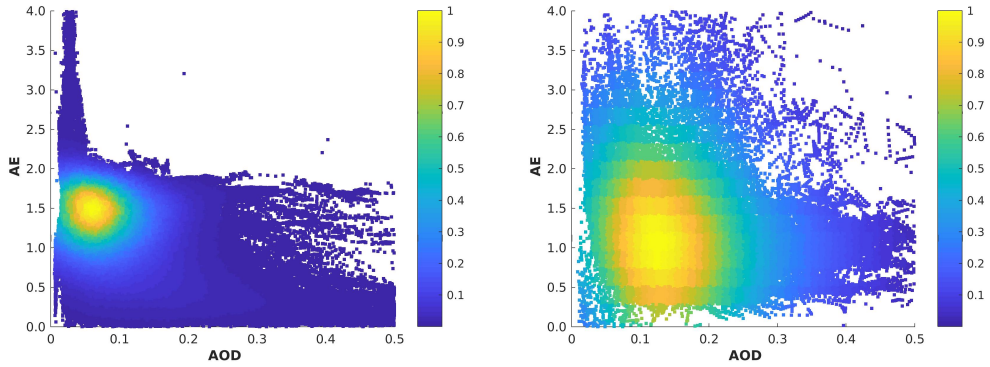

Figure 10. Density plot of AOD and Ångström Exponent (AE) for Sun (**left**) and star photometer (**right**) for all individual measurements from 2004 to 2023

For the sun photometer data, most observations accumulate in a very small range of AOD- and AE-values with $\tau \in [0.02, 0.1]$ and corresponding $AE \in [1.2, 1.7]$. A band of small aerosols and low AOD is found ($AE \rightarrow 4, \tau < 0.05$). The AOD in this regime is very

low, which results in a large uncertainty. This error propagates through the calculation of the Ångström Exponent, and hence, these values cannot fully be trusted. Individual events with high AOD and comparably large AE are also found. Since no averaging was applied to the data displayed in Figure 10, much more points are visible compared to Figure 9.

The situation is different for the star photometer. As already seen in Figure 5, the AOD is much larger than during solar measurements, with a corresponding lower AE. Typical combinations for the star photometer are $\tau \in [0.09, 0.3]$ and $AE \in [0.4, 1.8]$.

A more detailed overview of monthly median AE values is given in Figure 11 for the entire measurement period in grey. In orange over all these 20 years the lines for median (solid) and mean (dashed) are plotted. A more detailed distribution characteristics of the Ångström Exponent is presented in Figure 12. Generally, aerosols in the atmosphere above Ny-Ålesund are larger in winter times with a corresponding higher AOD than in summer times. The same result was also found by Gogoi et al. [37], who measured scattering coefficients at the surface.

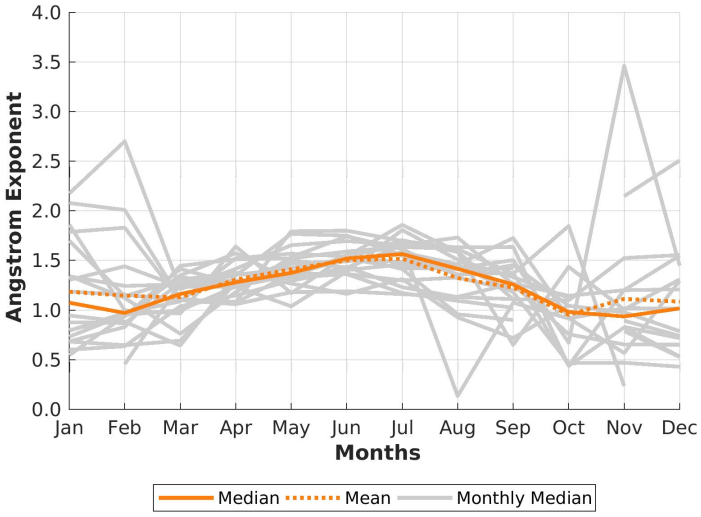

Figure 11. Monthly median values of the Ångström Exponent is shown in grey for all of the years 2004 to 2023. The median (solid) and mean (dashed) of these annual cycle is given in orange.

For the entire measurement period, it can be said that summers usually have a smaller monthly variability than winters. A generally increased AE in April and May compared to other months of the same year cannot clearly be seen in the data, which would be expected for a clear Arctic Haze season. The exceptionally low AE values, and therefore large particles, in August correspond to a wildfire event the year 2019 [29].

Summer exhibits smaller particles, with monthly median AE values typically between 1.2 and 1.7 (July), indicating a shift towards smaller aerosol sizes. The variability within a month reaches its maximum in July with low values, which indicate small particles on average. A small year-to-year variability evolves from June onwards with increasing tendency towards autumn and winter. The transition from summer to winter in September shows a gradual increase in particle size and variability.

After the polar day is over, a clear change in Ångström Exponent can be observed. Winters (October to February) are characterised by large particles with AE close to 1. There is significant diversity in the monthly median AE, with values in November ranging from 0.5 to 2.1. This is due to a wide variation in particle size during winter and especially in November. From November to January, a decreasing tendency in AE values is observed, indicating that particles became larger with decreasing variability from 2019 to 2023. The overall pattern suggests that aerosols arriving in the Arctic during winter, become more homogeneous (smaller spreading within a month) over time, with a consistent increase in AOD. When $AE \to 0.5$ the mean AOD is high ($\tau > 0.3$) and reduced with smaller AE. This

indicates that large particles are transported into the Arctic, resulting in a local increase of the optical depth there.

Spring (March and April) shows a relatively small year-to-year variability and monthly variation in aerosol sizes. However, an expected increase in AE during April, indicative of the Arctic Haze season, is not clearly observed, but rather a smooth transition from winter to summer.

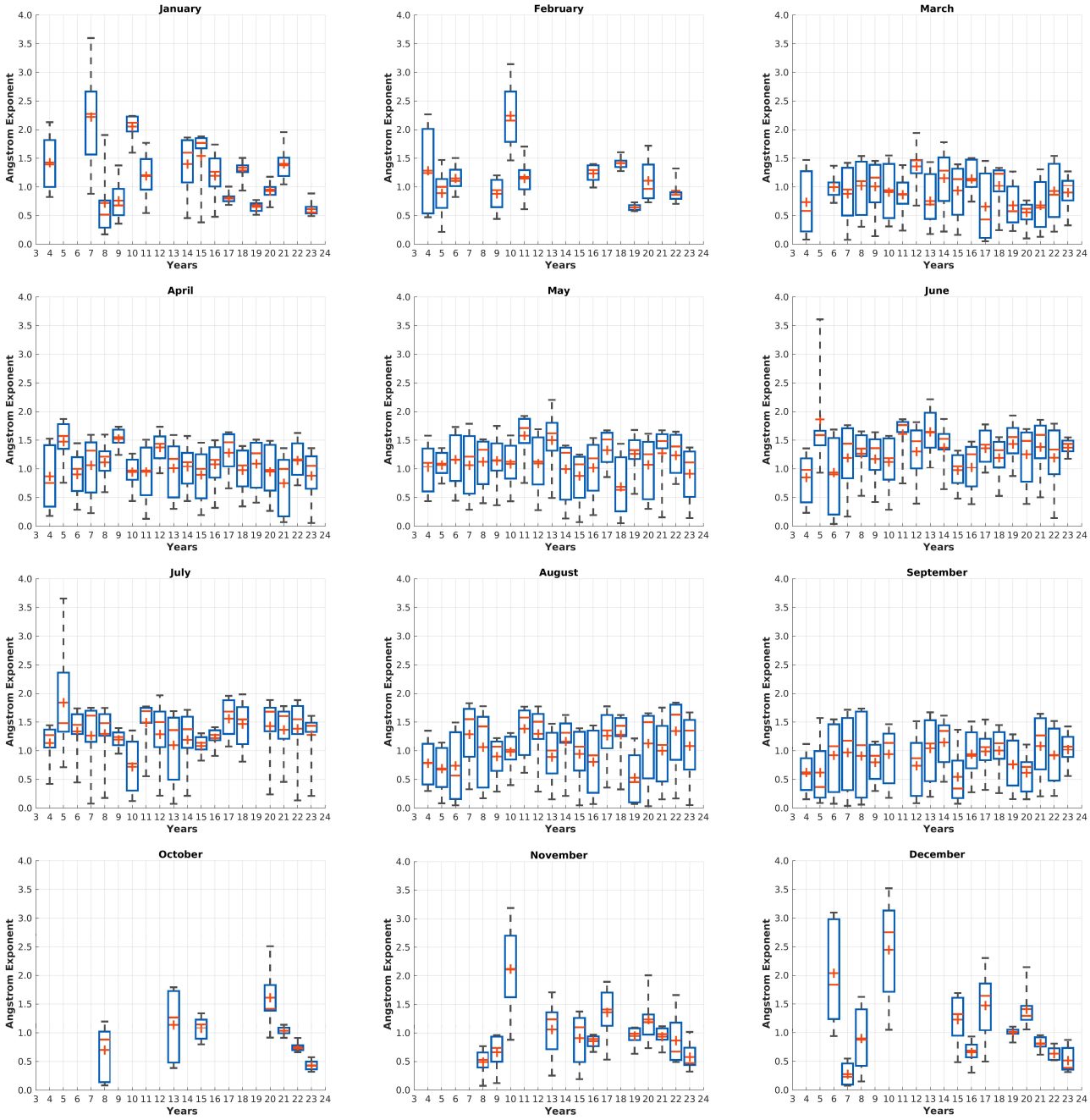

Figure 12. Box-and-whisker plots for Ångström Exponent for every month measured by sun and star photometer. All individual data points after cloud screening are taken into account. As a reference for the amount of data per month and year, see Table 1. The 25th and 75th percentile are shown by the blue boxes, whiskers indicate the 9th and 91st percentile, and the median is shown by − and mean by +.

5.6. Trend Analysis for Ångström Exponent

For every month, the mean AE value was calculated to deseasonalize the Ångström Exponent. With this deseasonalized AE, the deviation between every single monthly median and its corresponding monthly mean value are calculated. The result is shown in Figure 13.

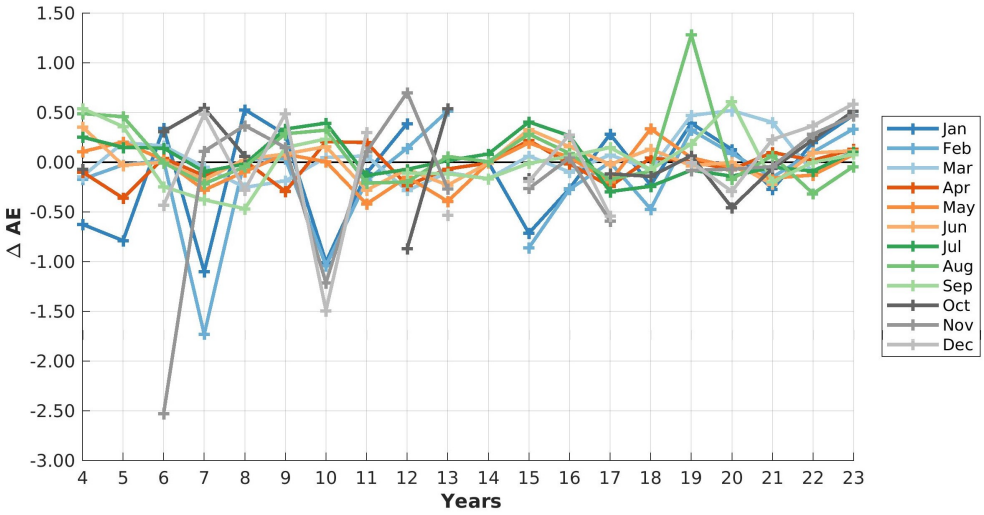

Figure 13. Deviation from monthly AE mean values to long-term median AE values.

For months with $\Delta AE < 0$, the observed aerosols had above-average effective sizes, for cases with $\Delta AE > 0$ vice-versa. The variability of ΔAE was large at the beginning of the observation time. But is decreasing from year to year (for all 12 months). The trend of the monthly mean AE, the Std (standard deviation of this parameter), and the 2σ confidence interval (uncertainty of the linear trend) are shown in Table 3.

A trend analysis is only possible to be performed with a 20-year-long data set, because the variability (indicated by the standard deviation and the 2σ confidence interval) is so large, that a potential trend is hidden behind it. The uncertainty parameters (Std and 2σ) are very large; therefore, trends of the parameter AE have to be analysed carefully. Positive trends in the parameter AE (see Table 3) mean that the particle size of the aerosols is decreasing. Negative trends in the parameter AE mean, that there is an increasing particle size. This occurs mostly in winter. The interpretation is that the particles transported over Ny-Ålesund in this season are getting larger from year to year.

Table 3. Deseasonalized linear monthly median AE trend and its standard deviation of the monthly median of AE for the years 2004–2023 with combined sun and star photometers. Positive values indicate aerosols becoming generally smaller over time. The 2σ interval is also given for uncertainty estimations.

	Jan	Feb	Mar	Apr	May	Jun	Jul	Aug	Sep	Oct	Nov	Dec
Trend	−0.55	−0.53	−0.17	−0.16	−0.04	0.03	0.23	0.20	−0.01	0.10	−0.91	−0.45
Std	0.52	0.53	0.23	0.16	0.19	0.17	0.20	0.36	0.28	0.39	0.77	0.55
2σ interval	1.15	1.28	0.42	0.36	0.46	0.35	0.36	0.68	0.58	0.85	1.74	1.24

In winter (November to February), aerosols tend to become larger, while a slight decrease in aerosol size is observed over the two decades in June to August. This trend needs to be considered with caution since for these months, the uncertainty parameters (Std and 2σ) are the highest. As already concluded in Section 5.2, the particles are more heterogeneous in winter, which can be supported by the analysis of the Ångström Exponent as well. The increase in AOD in autumn and early winter is caused by particles, which

become larger over time. The effective particle size increases not only in the winter, but also in March and April. Therefore, we do not conclude that the time of the Arctic Haze is shifted to earlier times. Rather we interpret that there is a general trend of increasing AOD and increasing particle size (decrease in AE) throughout the entire winter.

5.7. Duration of Events

With autocorrelation analysis a typical length of AOD events shall be determined for every month individually. Figure 14 shows the autocorrelations for each month in grey, ρ, and the median of the different years in green. An autocorrelation analysis was performed for a month, which fulfils the requirements discussed already in Section 4.3. For calculating the autocorrelation no interpolation was applied for measurement gaps.

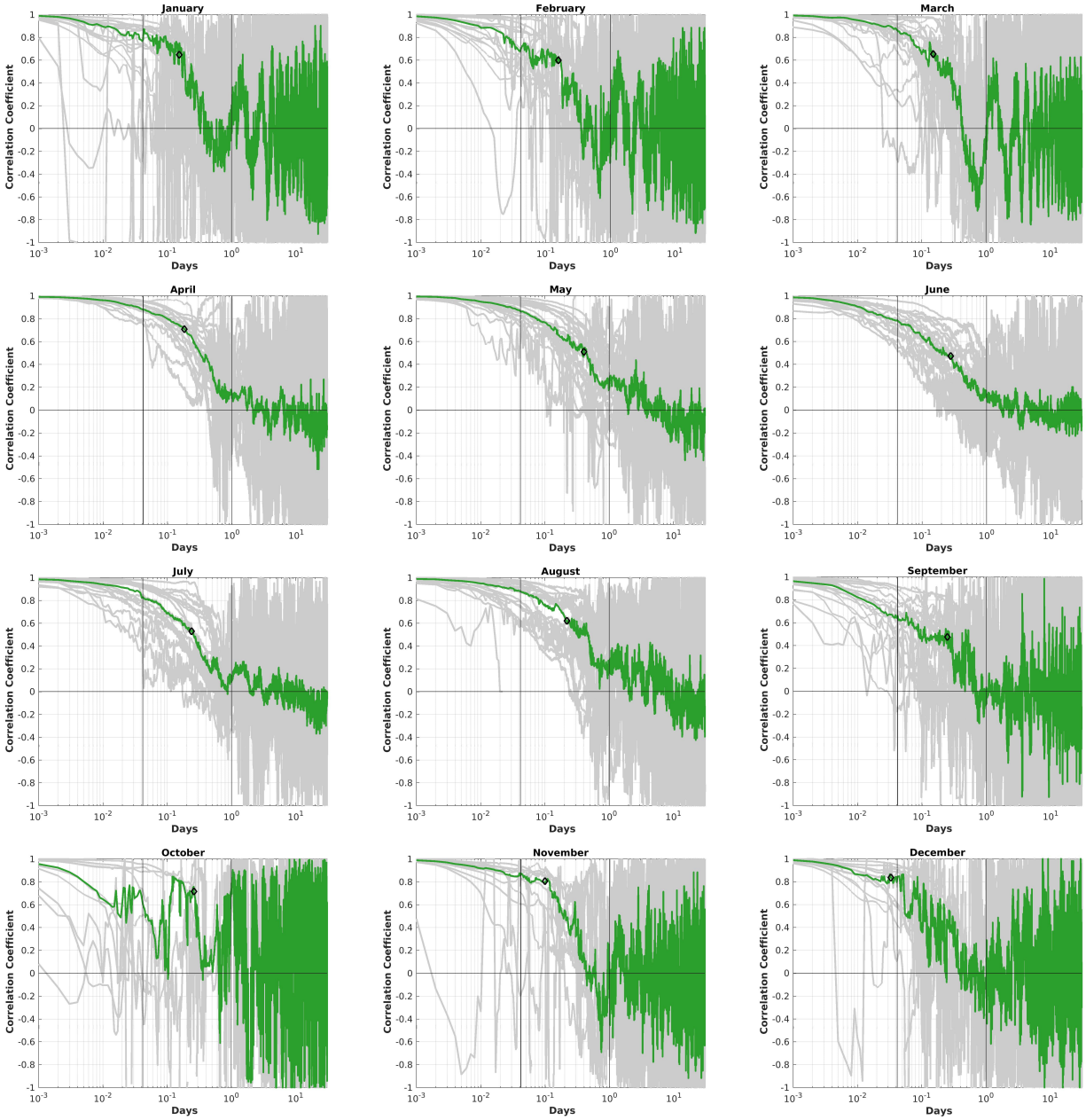

Figure 14. Autocorrelations for each month across the 20-year period (shown in grey) are displayed. The green line represents the median autocorrelation function derived from all individual monthly autocorrelations. Vertical lines indicate key time intervals at 1 h and 1 day. Additionally, black diamonds highlight the vertexes within the data.

Lags of 1 h and 1 day are each indicated by the black vertical lines. For all months, the variability between different years of one month is large as well as between adjacent months. For all months, the correlation coefficient decreases to $\rho < 0.2$ within the duration length of several hours. For every month, the vertex of the median curve (black diamond of Figure 14) is determined. This duration estimates a typical aerosol event of this month. The vertexes of in all months have a corresponding correlation coefficient in all cases > 0.47. The different time lags are shown in Table 4.

Table 4. Vertex of the median curve of the autocorrelation functions in Figure 14 for every month. The corresponding time lag is given in [h].

	Jan	Feb	Mar	Apr	May	Jun	Jul	Aug	Sep	Oct	Nov	Dec
Lag [h]	3.67	3.77	3.67	4.34	9.70	6.65	5.71	5.26	5.93	6.22	2.38	0.79

It can be seen that the duration is longest during the time between May and October and shortest throughout winter and spring (November to April). Generally a low variability occurs on minute time-scales. This indicates that aerosol events change significantly within usually about 3 h to 7 h. September and October have different patterns with a high variability within minute-scale, but this is due to the low data coverage (see Table 1). On time-scales of several days the correlation coefficient varies strongly, between −1 and +1. At that point, the atmosphere has no memory of previous events. Therefore, we conclude the observed events are all different from each other, especially during winter, the autocorrelation becomes noisy. However, for some months, a small positive correlation coefficient can be observed by 1.2 to 1.5 days with $\rho > 0.2$. A similar peak in ρ is also observed with a lower intensity in July to August with a similar length.

The more rapid decline of the median curve of the correlation coefficient between 1 h and 1 day in winter (November to March) indicates that consecutive aerosol events within one month are very diverse and no projection or forecast of their length or intensity can be made. These events also change rapidly. Sudden jumps in the correlation coefficient indicate larger gaps in the measurements, especially obviously in early winter. A smoother transition between consecutive aerosol events occur more often in summer, in which the decline of ρ happens on larger time scales, which indicates a smoother transition from low aerosol load to an event. The obtained duration of aerosol events agrees with the study by Dada et al. [38], who analysed aerosol events caused by warm air mass intrusions. Overall the duration of a single event of depends strongly on the atmospheric conditions [39].

5.8. Possible Aerosol Sources and Sinks

To investigate potential sources and sinks for high and low aerosol events in the Arctic, ten different potential contributors were investigated on their impact to the photometer observations. Therefore, a multiple linear regression analysis is performed using the implemented MATLAB-routine "regress.m". Note that the linear independence of these parameters was not checked. After the multiple linear regression analysis was performed, an artificial AOD was reconstructed, based on the result. This reconstructed AOD was afterwards correlated with the measured one for comparison. We used the following parameters:

- **PNA-** (Pacific-North American teleconnection pattern) and **NAO-Index** (North Atlantic Oscillation) by the Climate Prediction Center (last accessed on 6 June 2024): The NAO- and PNA-Indices are calculated daily and are based on Rotated Principal Component Analysis and are applied to monthly standardised 500 mbar height anomalies
- **Fire Radiative Power (FRP)** by MODIS–Moderate Resolution Imaging Spectroradiometer (last accessed on 6 June 2024): MODIS is a NASA satellite-based radiometer. It is designed for Earth observations across 36 different spectral bands, ranging from 0.4 µm to 14.4 µm in wavelength. Depending on the selected specific bands, MODIS offers a spatial resolution of 0.25° × 0.25° and a temporal resolution of approximately

two days. MODIS detects wildfires by analysing the 4 µm and 11 µm bands, identifying temperature anomalies relative to the background and absolute temperatures. This study uses the Fire Radiative Power (FRP) from the two satellites Aqua and Terra, with a gridded spatial resolution of 1 km. For more information about MODIS and its data products, visit the official website: MODIS–Moderate Resolution Imaging Spectroradiometer (last accessed on 3 October 2024)

- **Arctic Sea Ice Extend** by Meereisportal [40] (Data received by authors on 19 January 2024): The sea ice extend is a product of several, homogenised data sets from different passive microwave sensors of satellite observations with horizontal resolutions between 5 km to 50 km. More information can be found at Online Sea-Ice Knowledge and Data Platform (last accessed on 3 October 2024)
- **Radiosonde** products (temperature (T), pressure (P), wind speed (Wind Speed) and water vapour mixing ration (water vapour)) are described in detail by Maturilli and Kayser [41], Maturilli [42]. At AWIPEV, one radiosonde is launched at 11 UT every day. The altitude, in which the wind is less perturbed by orography is at about 700 m as it is shown by Graßl et al. [43] using Wind Lidar measurements. For taking local weather effects into account, we used these radiosonde observations
- **Precipitation** observations are taken from Met Norway (last accessed on 3 October 2024). A day with precipitation was chosen, if the daily cumulative amount was $\geq$1 mm.

The North Atlantic Oscillation depends on the strength and positions of Iceland Low and Azores High. In the positive phase both pressure systems are well evolved and the large-scale weather systems pass quickly. The meridional transport is weaker in the North Atlantic sector, which also prevents aerosols reaching the Arctic over this pathway. In a negative phase, both pressure systems are weak, blocking occurs. Continuously cold Arctic air reaches the midlatitudes or warm Atlantic air penetrates into the Arctic.

The PNA has a big influence on the extratropics on the Northern Hemisphere. The positive phase is associated with an enhanced East Asian jet stream with its exit over the western part of the USA with precipitation anomalies, including above-average amounts in the Gulf of Alaska to the Pacific Northwestern USA, while the negative phase is associated with blocking activity over the high latitudes of the North pacific and a strong split-flow over the central North Pacific.

In the frame of a case study by Graßl and Ritter [9], we tested the hypothesis with a longer time series that sea ice prevents removal processes of aerosols from the lower atmosphere. Another explanation for a positive correlation between sea ice extend and AOD could be the erosion of ice crystals by wind. These ice crystals are then further transported and measured in Ny-Ålesund. To test this hypothesis, depolarisation measurements of aerosols are be needed. This information is not available with both photometers of this study and therefore has to be performed in future studies.

On a regular basis, wildfires occur in the Northern Hemisphere throughout the entire year and are a big source for aerosols, which can be lifted by several processes into the free troposphere or even stratosphere, where they are able to be transported over long distances [44–46]. Since Russia and North America represent the two major land masses, where large wildfires on the Northern Hemisphere occur, these regions are represented in the rectangular fields by the geographical coordinates 77°N 31°E and 48°N 180°E for "Russia" and by 71°N 170°W and 48°N 52°W for "North America" (NA).

Assuming that aerosols are a good tracer of wind fields, the altitude of 700 m is used to compare the photometer data with local atmospheric conditions. For this study, monthly mean profiles were taken and compared with monthly mean AOD measurements. Temperature and pressure are taken into account, since they are good tracers for pressure systems moving over Ny-Ålesund but also warm air intrusions, which might also affect the aerosol budget.

As Schmale et al. [14] has already shown, the Arctic aerosol budget is influenced by several different parameters. Hence, a correlation analysis between each independent

parameter and the measured AOD would lead to wrong conclusions. The obtained parameters are then used to construct an AOD, which is expected to be measured, if the chosen ten parameters are responsible for the aerosol budget. A correlation analysis afterwards shows how well the artificially obtained AOD matches to the observations. Monthly median values of NAO, PNA, pressure, temperature and wind speed at 700 m altitude, integrated water vapour over the entire troposphere, sea ice cover of the Arctic, precipitation days and wildfires in North America and Russia.

The parameter coefficients for the above-mentioned parameters of the multiple linear regression are shown in Table 5. Since sea ice cover is in the order of magnitude of 10^8 km^2 but NAO- or PNA-indices are usually <2, a normalisation was applied before calculating the regression parameters. The normalisation factors of each parameter are also given, as well as the upper and lower confidence intervals.

As shown in Table 5, the coefficients of the multiple linear regression analysis are different for each chosen period. Early spring (March and April) are in direct comparison still a bit different, which also agrees with the previous findings of our study. The negative sign for fire radiative power (FRP) for North America and Russia might be a bit counter intuitive. We think, the highly polluted air by boreal wildfires either has no trajectories into the European Arctic or the aerosol is dry or wet removed before arriving at Svalbard. The positive coefficient between sea ice cover and AOD agrees to the study by Graßl and Ritter [9] with a significantly larger data set. With these coefficients of Table 5, we conclude that the measured aerosol load throughout the time period 2004–2023 is a superposition of different sources and sinks as well as different pathways into the Arctic. A clear correlation between an AOD event and a source or pathway was not found.

Table 5. Normalised coefficients of the multiple linear regression are shown. Due to the large span between the different parameters in the order of magnitudes, these parameters were first normalised to a range between $[-1, +1]$ for a better comparison between each other. Afterwards the multiple linear regression was calculated with these normalised values. The order of magnitude for the normalisation is given in $[\cdot]$. Additionally, the confidence lower and upper intervals for each period is given in $(\cdot)$.

	NAO $[\times\mathbf{10}]$	**PNA** $[\times\mathbf{10}]$	**P** $[\times\mathbf{10^3}]$	**T** $[\times\mathbf{10^3}]$	**Water Vapour** $[\times\mathbf{1}]$	**Wind Speed** $[\times\mathbf{10^2}]$	**Sea Ice Cover** $[\times\mathbf{10^8}]$	**Precip Days** $[\times\mathbf{10^2}]$	**FRP (NA)** $[\times\mathbf{10}]$	**FRP (RU)** $[\times\mathbf{10}]$
Mar–Apr	−0.04 (−0.22) (0.13)	−0.18 (−0.34) (−0.01)	−0.39 (−2.08) (1.30)	0.19 (−5.62) (6.01)	−0.20 (−0.46) (0.06)	0.38 (−0.39) (1.15)	2.73 (−0.08) (5.54)	−0.72 (−1.32) (−0.11)	0.34 (0.00) (0.68)	0.04 (−0.96) (1.03)
May–Sep	−0.09 (−0.23) (0.05)	0.07 (−0.10) (0.25)	2.29 (0.19) (4.38)	−6.28 (−13.44) (0.88)	0.07 (−0.04) (0.17)	−0.38 (−1.34) (0.57)	−1.03 (−2.27) (0.21)	−0.15 (−0.67) (0.36)	−0.11 (−0.30) (0.08)	−1.02 (−2.17) (0.13)
Oct–Feb	0.12 (−0.14) (0.37)	0.09 (−0.12) (0.30)	0.75 (−2.08) (3.78)	−2.05 (−11.85) (7.76)	−0.16 (−0.47) (0.16)	−0.60 (−2.19) (0.99)	0.79 (−0.30) (1.89)	−0.07 (−0.56) (0.49)	−0.05 (−0.30) (0.20)	−0.05 (−0.47) (0.37)
Jan–Dec	0.02 (−0.08) (0.13)	0.10 (−0.01) (0.22)	1.50 (0.32) (2.68)	−5.01 (−9.00) (−1.02)	0.02 (−0.07) (0.12)	0.23 (−0.41) (0.87)	0.35 (−0.22) (0.92)	0.17 (−0.13) (0.47)	−0.02 (−0.14) (0.11)	−0.02 (−0.37) (0.33)

Figure 15 shows the measured AOD median and the reconstructed AOD based on the above-mentioned parameters after performing a multiple linear regression.

The observed and the reconstructed AOD-curves are further correlated with each other to obtain an estimation about the alignment between each other. The chosen parameters for the multiple linear regression analysis represent different seasons with a different signs and order of magnitude for the selected months or in total. Figure 15 shows a good reconstruction for years without extreme AOD events, such as from 2009 to 2014. In other years

with exceptional high AOD values, this simulation does not provide a good reconstruction. In these cases, the measured AOD is much higher than the reconstructed one.

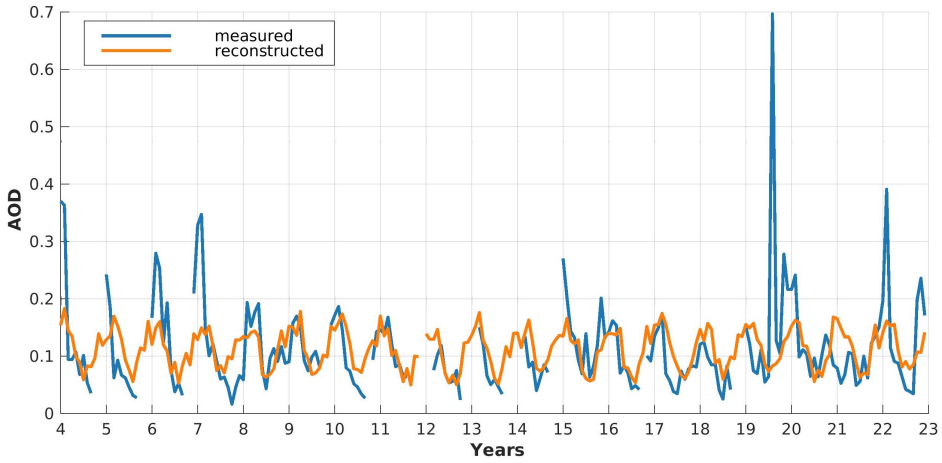

Figure 15. Monthly median AOD values are given in blue. With a multiple linear regression this AOD is reconstructed by using the above-mentioned parameter coefficients.

For all months, a correlation coefficient $\rho = 0.43$ (p-value: 10^{-10}) was found. By just looking at individual time periods the situation is different: while March and April can be reconstructed well ($\rho = 0.62$, p-value: 10^{-5}), summer is poorer represented with a correlation $\rho = 0.35$ (p-value: 10^{-4}). Winter is close to the annual correlation $\rho = 0.48$ (p-value: 10^{-5}). The small p-values in all seasons and the entire year indicate that the used set of possible sources and sinks do not span a full orthogonal basis, on which the multiple linear regression analysis is calculated because the correlation is not significant. A high correlation between the reconstructed and observed AOD indicates a large contribution by the chosen parameters to the aerosol budget at Ny-Ålesund. With this set of different parameters, the observed AOD cannot be represented entirely. This can be caused by the presence of more local sources and agrees with in situ measurements by Tunved et al. [47]. Generally speaking, the full annual cycle can partially be explained by the chosen parameters and the correlation could be improved by using slightly different variables, with which the AOD is reconstructed.

6. Discussion

The study by Tunved et al. [47] found out with aerosol in situ measurements that the particle formation of small particles starts in April and reaches its annual maximum in June, while simultaneously the number concentration of larger particles is slowly decreasing. The minimum is reached in October for small and large aerosol size ranges. The newly formed particles seem to grow relatively slowly compared to other observations outside of the Arctic. During January and February, aerosols are persistent within accumulation mode. A larger variability returns to the aerosol size distribution in March together with the end of the polar night. From June to August, a clear sign of local particle formation and growth was found, which ends with the end of the polar day in September.

The aerosol number concentration is smallest during October and increases afterwards until it reaches its local maximum in April and has an impact on the largest spread of the monthly median values, which the star photometer detected. A mode in the aerosol size distribution with an effective radius around 150 nm evolves from October onwards and peaks in April. The beginning of particle formation by the presence of polar day in May changes the abundance of aerosols within weeks and cannot be purely explained by changes in transport pathways of the arriving air masses. It is more likely that these changes are linked to increased wet removal and enhanced photochemical processes [48]. The lack of large aerosols might be caused by the combination of dry deposition and wet scavenging,

which might be more efficient in summer than in winter [48]. These studies follow the observations of the sun photometer nicely and are confirmed by the calculations of the Ångström Exponent, which reaches its annual maximum in July. The studies of Tunved et al. [47], Garrett et al. [49] agree very well with our observations in AOD, Ångström Exponent as well as the autocorrelation analysis, where small particles are observed with a simultaneously increased frequency of local events.

As already stated in Garrett et al. [48,49], we found a very similar annual cycle of aerosol abundance compared to the North American places Alert, Canada, and Barrow, USA. For these studies, air surface CO-measurements were taken from 2000–2009. With these measurements, a scavenging factor was calculated, which is indirect proportional to the aerosol concentration in the Arctic lower troposphere. Since CO and aerosols are affected by dilution but CO is able to form chemical compositions, the ratio between CO and aerosol concentration can be used as an indicator for aerosol dry and wet removal. If the ratio maintains its source value, the aerosol concentration variability is driven by dilution or mixing. More details and the assumptions are given in Garrett et al. [48].

As well as in the presented study with photometer measurements a strong seasonal cycle was found with this method. As also pointed out by Garrett et al. [49], the origin of this cycle is not primarily in changes in transport efficiency but rather in removal processes of aerosols on their pathway to the Arctic. This also explains the missing or even negative correlation with strong aerosol sources, like wildfires in Russia or North America.

The modelling study by Quinn et al. [6] revealed that during an NAO positive phase, the effective transport of aerosol tracers becomes more enhanced especially during winter and spring. In direct comparison with the negative phase, the efficiency is increased by up to 70%. Since trace gases cannot be dry or wet deposited, unlike aerosols, CO is a good tracer of long-range pollution pathways into the Arctic. Eckhardt et al. [50] also found a correlation between the positive NAO phase and high concentrations of CO mainly originating from Europe and less from North America. This result cannot be directly confirmed by our analysis, because NAO and PNA have a small contribution to the reconstructed AOD. Other parameters, like local temperature and pressure as well as sea ice cover have a larger impact.

In the model study of Rinke et al. [51] analysing the years 1979–2015, it was shown that 20 to 40 extreme cyclones occur in the Arctic North Atlantic per winter season with an increasing trend of 3–4 events per decade for the months November and December. With an increasing number of (extreme) cyclones reaching the Arctic, circulation patterns change within and therefore the relative humidity as well as aerosol pollution pathways and their lifetime. With the limitations of the clear-sky bias of both photometers, this model study agrees very well with the results of this trend analysis since we also observed a strong increase in τ in October to December, with over the entire period small trend in January.

In the study of You et al. [52] using ERA5 reanalysis data from 1979–2018, an increasing trend of moisture and heat transport over Beaufort Sea into the Arctic was found during winter with a simultaneously increasing occurrence of blocking days. During summer, the enhanced poleward transport of energy and heat takes place more frequently in the East Siberian Sea sector. Due to the geographical location of Ny-Ålesund, the station is less affected by this summer trend. The photometers at Ny-Ålesund rather see air from the inner Arctic, where the numbers of aerosol sources are comparably small.

The study by Yao et al. [53] uses space-born level 3 Lidar data by Cloud-Aerosol Lidar with Orthogonal Polarization (CALIOP) for the seasonal AOD and composition of tropospheric aerosols in the Arctic during day and night time between 2007 and 2019. The study reveals that the Arctic is generally more polluted during winter (December to February) than during summer. Together with reanalysis data by Modern-Era Retrospective analysis for Research and Applications, Version 2 (MERRA-2), the contribution of different aerosol types are shown for each season by Yao et al. [53]. The modelled total AOD fits very well with our observations in Ny-Ålesund with an AOD maximum in winter and a minimum in summer.

While sea salt is the most dominant type in winter (December to February), the contribution decreases and reaches its minimum in summer (June to August). In spring (March to May), the dominant aerosol type changes to sulfate with some dust contributing to the total AOD. Black and organic carbon is usually transported Svalbard over the North Pole during summer months. In autumn (September to November) sulfates and sea salt are the main contributors. The large aerosols are associated with sea salt and dust, while sulfate as particles in nucleation mode are comparably small [47,48,54]. These results agree with our observations of the annual cycle of aerosol properties measured continuously by photometers in Ny-Ålesund.

7. Conclusions and Outlook

We presented in this study a homogenised data set from sun and star photometer measured in Ny-Ålesund in the European Arctic. The aim was not to focus on a special or extreme event of high AOD (e.g., volcanic eruption, huge wildfire event), but to investigate the general trends in aerosol load (AOD) and aerosol particle size (AE). Our key findings are:

- A homogenised data set from sun and star photometer is crucial to observe strong inter-annual, seasonal and short-term changes in the aerosol load and properties in high latitudes.
- The AOD dataset from sun and star photometers matches well with in-situ AOD measurements from the same site. It also shows similarities to other American Arctic sites, like Barrow or Alert, pan-Arctic satellite observations and reanalysis data investigations. The data reveals some key features of the Arctic atmosphere, with large particles during the winter, and during the summer, often lower AOD and smaller particles (larger AE). These features are not unique to the measurement site, but suits to an Arctic-wide phenomenon. PSC optical depth estimated with the Lidar method is smaller than 0.06. This demonstrates that PSC are not the only reason of the trend of increasing AOD observed with the star photometer during the winter.
- A subtle trend can be found in two decades of sun and star photometer observations with increasing AOD in winter months and a simultaneous decreasing tendency in spring. Therefore, the Arctic Haze is expected to become weaker or rarer in the years to come. Since many aerosol events are recorded by the star photometer, it is definitely necessary to extend the sun photometer data set by star and lunar measurements to obtain a better understanding of the polar atmosphere during the entire year, since winter dimming is expected to be more and more pronounced.
- With several different large-scale oscillations (PNA, NAO), local atmospheric parameters (temperature, wind speed, pressure, precipitation days) and wildfires in Russia and North America, we reconstructed an AOD and compared to the measured AOD. Especially in spring and years without major aerosol events, the result was good. The spring AOD is therefore most dominated by the given parameters. In summer, when local sources become more and more important, the comparison results showed that the simulation was less successfully.
- The AOD observed in Ny-Ålesund and over the Arctic in general is dominated by long-range transported aerosols and having their sources during processes that occur far away from the Arctic region. Hence, pathways into the Arctic as well as possible sinks and additional sources during transportation are important to understand the properties of the aerosols observed at Ny-Ålesund.

The long dataset shows the importance of long-term monitoring of the polar atmosphere, since trends are very subtle recognisable. In future studies, the results could be compared with other long-term photometer observations from other Arctic sites. This study also emphasises the importance of aerosol measurements during the polar night with automatic and continuous observations. March and October usually have the problem that both instruments have a very limited measurement window per day and the data coverage is poorer than in other months. To fill this gap, a moon photometer might help for several

days around full moon, when the Sun is at the same time sufficiently below the horizon. Additionally, a moon photometer is cheaper, less bulky and easier to use (full automatic) than a star photometer. It can therefore be more easily performed at remote places in the Arctic. To bring both instruments and the interpretation of their measurements better together, a scanning Lidar would be preferable, since then measurements right beside the celestial object can be performed during the entire year. With this instrument, we can focus on the observations in the direction of the celestial object observed by the photometers (Sun, Moon or observed stars) during the entire year, filling data gaps of the photometers, giving additional information (profile distribution) or allowing Lidar-Photometer comparison on the AOD.

Aerosol properties, load, concentration and appearance are crucial for improving climate model predictions, but also assessing non-linear aerosol-radiation-cloud interactions in the Arctic. With an improved understanding of Arctic aerosols, the evolution of ongoing environmental changes in the Arctic can further be investigated and better understood.

Author Contributions: Conceptualization, S.G. and C.R.; methodology, S.G. and C.R.; software, S.G. and J.W.; validation, S.G. and J.W.; formal analysis, S.G. and R.H. (Regularisation of Lidar data); investigation, S.G.; data curation, S.G. and J.W.; writing—original draft preparation, S.G.; writing—review and editing, S.G., L.D., C.R. and R.R.; visualization, S.G.; supervision, C.R. and S.G. All authors have read and agreed to the published version of the manuscript.

Funding: Part of this work was supported by the COST Action Harmonia (CA21119: "International network for harmonisation of atmospheric aerosol retrievals from ground based photometers") supported by COST (European Cooperation in Science and Technology) https://harmonia-cost.eu/ (accessed on 3 October 2024).

Data Availability Statement: Sun photometer data can be found in the Pangaea data repository in the collection of https://doi.org/10.1594/PANGAEA.940018 accessed on 3 October 2024) [22]. Also most of the star photometer data can be found as a data collection on the Pangaea data repository https://doi.org/10.1594/PANGAEA.937903 (accessed on 3 October 2024) [24]. The data for the AO-, PNA- and NAO-indices were downloaded from NOAA (accessed on 3 October 2024). MODIS data are from MODIS Web (accessed on 3 October 2024) and the sea ice data from Meereisportal. Precipitation data originates from Met Norway (accessed on 3 October 2024).

Acknowledgments: The photometers were serviced at Ny-Ålesund by several Observatory Engineers at AWIPEV as well as by impres GmbH. Calibration at Tenerife, Spain, was regularly as well as the data checked (Potsdam, Germany) by Siegrid Debatin.

Conflicts of Interest: The authors declare no conflict of interest.

Appendix A. Error Estimation of the Star Photometer

A detailed error analysis about the sun photometer was performed by Stock [21]. We used the same procedure to estimate the error of the AOD for the star photometer accordingly. A more detailed analysis of star photometer errors are described by Ivănescu et al. [55]. The star photometer in their study is from the same type as ours and therefore the presented errors similar.

The star photometer measures the incoming star irradiance in photo counts, which are used to calculate the total optical depth. Since the raw signal of the sun photometer is given as a voltage, whereas the star photometer measures photo counts, we use use in this analysis the parameter Raw Signal, RS. Note that the parameter RS is an instrument specific variable with in our case 1 count/s $\widehat{=}$ 1500 photons received from the observed star. Equivalent to Stock [21], an error estimation of the star photometer was performed by estimating the largest error of all independent variables of the AOD calculation:

$$\Delta\tau_{aer}(\lambda) = \underbrace{\left|\frac{\partial\tau_{aer}}{\partial RS_0}\right|\Delta RS_0}_{t_1} + \underbrace{\left|\frac{\partial\tau_{aer}}{\partial RS}\right|\Delta RS}_{t_2} + \underbrace{\left|\frac{\partial\tau_{aer}}{\partial m_{aer}}\right|\Delta m_{aer}}_{t_3} + \underbrace{\left|\frac{\partial\tau_{aer}}{\partial\tau_{Ray}}\right|\Delta\tau_{Ray}}_{t_4} + \underbrace{\left|\frac{\partial\tau_{aer}}{\partial m_{Ray}}\right|\Delta m_{Ray}}_{t_5} + \underbrace{\left|\frac{\partial\tau_{aer}}{\partial\tau_{O_3}}\right|\Delta\tau_{O_3}}_{t_6} + \underbrace{\left|\frac{\partial\tau_{aer}}{\partial m_{O_3}}\right|\Delta m_{O_3}}_{t_7} \quad \text{(A1)}$$

with RS_0 and RS the raw signal from calibration and measurement measured by the photometer, respectively, the airmass m and optical depth τ for the contribution of aerosols, *aer*, Rayleigh scattering, *Ray*, or Ozone absorption O_3, respectively.

Observation of 17 December 2020 is used for the following estimation of the absolute error, since on this day the atmospheric conditions were very stable and a long observation was performed. The relative contributions of each of the terms of Equation (A1) is shown in Table A1. On this day, a mean AOD of $\tau_{420} = 0.14$, $\tau_{500} = 0.11$ and $\tau_{1025} = 0.09$ was measured. We used $\Delta\lambda = \pm 0.002$ nm based on the information given by the manufacturer of the instrument, an error in ozone column concentration of $\pm 3\%$, an error in the calculation of the star elevation by $\pm 0.05^\circ$ according to Stock [21] at an airmass between 1.9 and 2.1, and an uncertainty in the surface pressure measurement of ± 0.1 hPa. The error in the calibration raw signal, ΔRS_0, was calculated by the standard deviation this star during upper culmination and constant atmospheric conditions. For this star photometer, an error occurs during very stable atmospheric conditions of $\pm 72{,}000$ photons for $\lambda = 420.0$ nm, $\pm 16{,}500$ photons for $\lambda = 500.4$ nm and ± 750 photons for $\lambda = 1029.5$ nm was determined within the upper culmination of the star. The relative contribution [%] of all of the terms t_1 to t_7 of Equation (A1) to the entire error of $\Delta\tau_{aer}$ is given in Table A1.

Table A1. Relative contribution [%] of the single terms of Equation (A1) to the total error to the three exemplary wavelengths with the mean AOD of 17 December 2020 as a reference.

	t_1	t_2	t_3	t_4	t_5	t_6	t_7	AOD
420.0 nm	3.0	75.4	0.1	20.6	<0.1	0.0	0.0	0.14
500.4 nm	2.9	66.3	<0.1	11.2	<0.1	19.4	0.4	0.11
1029.5 nm	6.7	91.2	0.1	1.0	<0.1	0.0	0.0	0.08

The terms with the lowest relative contributions refer to errors in aerosol and Rayleigh air mass correction (t_3 and t_5, respectively) and the noise within the calibration process (t_1). The Rayleigh optical depth (t_4) is more critical for smaller wavelengths and less important for larger ones. Depending on the wavelength the ozone correction (t_6) contributes with >19% to the absolute error. By far the most important error is the signal-to-noise ratio (t_2). The absolute values of the largest error estimation are given in Table A2 for star and sun photometer in comparison.

Table A2. Largest error estimation for sun and star photometer in comparison for selected wavelengths. Error for sun photometer taken from Stock [21] for small airmasses.

	420.0 nm	500.4 nm	1029.5 nm
Sun photometer	0.02	0.01	0.01
Star Photometer	0.03	0.02	0.01

Since the AOD in the Arctic is generally low compared to more populated areas in the world, the importance of precise measurements of ozone optical depth is very important. Moreover, the ozone depletion takes place in the Arctic stratosphere. So, the column ozone concentration is generally different than in lower latitudes.

Appendix B. Sensitivity of the Star Photometer towards Errors in Raw Signal

To estimate the error of the new method for star photometer evaluation, let us assume a mean raw signal, $\overline{RS}$, during a very stable measurement period for the reference star 1. Star 2 shall be calibrated using Equations (1) and (2):

$$RS^2_{meas} = \overline{RS^2_0} \cdot 10^{-0.4(mag^2 - mag^1)} \tag{A2}$$

Let us assume a constant error during the measurement of the stellar apparent magnitudes of δ ($\Delta mag \rightarrow \Delta mag + \delta$). This error will propagate through the calculations and will create a factor to the calibration counts of star 2, $\widetilde{RS^2_{meas}}$:

$$\begin{aligned} \widetilde{RS^2_{meas}} &= \overline{RS^2_0} \cdot 10^{-0.4[mag^2 - (mag^1 + \delta)]} \\ &= \overline{RS^2_0} \cdot 10^{-0.4(mag^2 - mag^1) + 0.4\delta} \\ &= RS^2_{meas} \cdot 10^{+0.4\delta} \end{aligned} \tag{A3}$$

And with this also an additional term to the TOD of star 2, τ^2_{tot}:

$$\begin{aligned} \widetilde{\tau^2_{tot}} &= -\frac{1}{m_{tot}} \ln\left(\frac{RS^2_{meas}}{\widetilde{RS^2_0}}\right) \\ &= -\frac{1}{m_{tot}} \ln\left(\frac{RS^2_{meas}}{RS^2_0 \cdot \ln\left(10^{+0.4\delta}\right)}\right) \\ &= -\frac{1}{m_{tot}} \left[\ln\left(\frac{RS^2_{meas}}{RS^2_0}\right) - \ln\left(10^{+0.4\delta}\right)\right] \\ &= \tau^2_{tot} + \frac{\ln\left(10^{+0.4\delta}\right)}{m_{tot}} \end{aligned} \tag{A4}$$

The absolute error for AOD of the star photometer is according to the manufacturer $\Delta\tau_{tot} = 0.01$, which is surprisingly low. Therefore, we estimated an error as described in Appendix A. As it is further discussed by Stock [21], the error strongly depends also on the elevation of the celestial object and becomes most uncertain the lower the object is above the horizon.

References

1. Shaw, G.E. The Arctic haze phenomenon. *Bull. Am. Meteorol. Soc.* **1995**, *76*, 2403–2414. [CrossRef]
2. Heintzenberg, J.; Tuch, T.; Wehner, B.; Wiedensohler, A.; Wex, H.; Ansmann, A.; Mattis, I.; Müller, D.; Wendisch, M.; Eckhardt, S.; et al. Arctic haze over central Europe. *Tellus B Chem. Phys. Meteorol.* **2011**, *55*, 796–807. [CrossRef]
3. Hillamo, R.; Kerminen, V.M.; Maenhaut, W.; Jaffrezo, J.L.; Balachandran, S.; Davidson, C. Size distributions of atmospheric trace elements at Dye 3, Greenland—I. Distribution characteristics and dry deposition velocities. *Atmos. Environ. Part A. Gen. Top.* **1993**, *27*, 2787–2802. [CrossRef]
4. Radke, L.F.; Lyons, J.H.; Hegg, D.A.; Hobbs, P.V.; Bailey, I.H. Airborne observations of Arctic aerosols. I: Characteristics of Arctic haze. *Geophys. Res. Lett.* **1984**, *11*, 393–396. [CrossRef]
5. Brock, C.A.; Radke, L.F.; Lyons, J.H.; Hobbs, P.V. Arctic hazes in summer over Greenland and the North American Arctic. I: Incidence and origins. *J. Atmos. Chem.* **1989**, *9*, 129–148. [CrossRef]
6. Quinn, P.K.; Shaw, G.; Andrews, E.; Dutton, E.; Ruoho-Airola, T.; Gong, S. Arctic haze: Current trends and knowledge gaps. *Tellus B Chem. Phys. Meteorol.* **2007**, *59*, 99–114. [CrossRef]
7. Shaw, G.E.; Stamnes, K. Arctic haze: Perturbation of the polar radiation budget. *Ann. N. Y. Acad. Sci.* **1980**, *338*, 533–539. [CrossRef]
8. Maturilli, M.; Herber, A.; König-Langlo, G. Surface radiation climatology for Ny-Ålesund, Svalbard (78.9 N), basic observations for trend detection. *Theor. Appl. Climatol.* **2015**, *120*, 331–339. [CrossRef]
9. Graßl, S.; Ritter, C. Properties of Arctic Aerosol Based on Sun Photometer Long-Term Measurements in Ny-Ålesund, Svalbard. *Remote Sens.* **2019**, *11*, 1362. [CrossRef]
10. Haywood, J.; Donner, L.; Jones, A.; Golaz, J.C. *Global Indirect Radiative Forcing Caused by Aerosols: IPCC (2007) and Beyond*; MIT Press: Cambridge, MA, USA, 2009. [CrossRef]

11. Artaxo, P.; Bretherton, C.; Feingold, G.; Forster, P.; Kerminen, V.-M.; Kondo, Y.; Liao, H.; Lohmann, U.; Rasch, P.; Satheesh, S.K.; et al. Climate Change 2013: The Physical Science Basis. In *IPCC-Intergovernmental Panel on Climate Change*; Cambridge University Press: New York, NY, USA, 2014.
12. Bauer, S.E.; Tsigaridis, K.; Faluvegi, G.; Kelley, M.; Lo, K.K.; Miller, R.L.; Nazarenko, L.; Schmidt, G.A.; Wu, J. Historical (1850–2014) aerosol evolution and role on climate forcing using the GISS ModelE2. 1 contribution to CMIP6. *J. Adv. Model. Earth Syst.* **2020**, *12*, e2019MS001978. [CrossRef]
13. Masson-Delmotte, V.; Zhai, P.; Pirani, A.; Connors, S.; Péan, C.; Berger, S.; Caud, N.; Chen, Y.; Goldfarb, L.; Gomis, M.; et al. (Eds.) *Climate Change 2021: The Physical Science Basis*; Cambridge University Press: New York, NY, USA, 2021; p. 2391. [CrossRef]
14. Schmale, J.; Sharma, S.; Decesari, S.; Pernov, J.; Massling, A.; Hansson, H.C.; Von Salzen, K.; Skov, H.; Andrews, E.; Quinn, P.K.; et al. Pan-Arctic seasonal cycles and long-term trends of aerosol properties from ten observatories. *Atmos. Chem. Phys. Discuss.* **2021**, *22*, 3067–3096. [CrossRef]
15. Pernov, J.B.; Beddows, D.; Thomas, D.C.; Dall' Osto, M.; Harrison, R.M.; Schmale, J.; Skov, H.; Massling, A. Increased aerosol concentrations in the High Arctic attributable to changing atmospheric transport patterns. *Npj Clim. Atmos. Sci.* **2022**, *5*, 62. [CrossRef]
16. Herber, A.; Thomason, L.W.; Gernandt, H.; Leiterer, U.; Nagel, D.; Schulz, K.H.; Kaptur, J.; Albrecht, T.; Notholt, J. Continuous day and night aerosol optical depth observations in the Arctic between 1991 and 1999. *J. Geophys. Res. Atmos.* **2002**, *107*, AAC 6-1–AAC 6-13. [CrossRef]
17. Tomasi, C.; Kokhanovsky, A.A.; Lupi, A.; Ritter, C.; Smirnov, A.; O'Neill, N.T.; Stone, R.S.; Holben, B.N.; Nyeki, S.; Wehrli, C.; et al. Aerosol remote sensing in polar regions. *Earth-Sci. Rev.* **2015**, *140*, 108–157. [CrossRef]
18. Gilardoni, S.; Heslin-Rees, D.; Mazzola, M.; Vitale, V.; Sprenger, M.; Krejci, R. Drivers controlling black carbon temporal variability in the lower troposphere of the European Arctic. *Atmos. Chem. Phys.* **2023**, *23*, 15589–15607. [CrossRef]
19. Pasquier, J.T.; David, R.O.; Freitas, G.; Gierens, R.; Gramlich, Y.; Haslett, S.; Li, G.; Schäfer, B.; Siegel, K.; Wieder, J.; et al. The Ny-Ålesund aerosol cloud experiment (nascent): Overview and first results. *Bull. Am. Meteorol. Soc.* **2022**, *103*, E2533–E2558. [CrossRef]
20. WMO Group. *Guide to Meteorological Instruments and Methods of Observation*; WMO Library: Geneva, Switzerland, 1996.
21. Stock, M. Charakterisierung der Troposphärischen Aerosolvariabilität in der Europäischen Arktis. Ph.D. Thesis, Universität Potsdam, Potsdam, Germany, 2010.
22. Graßl, S.; Ritter, C. Sun Photometer Data (RAW) from Ny-Ålesund, Svalbard (AWIPEV). 2022. Available online: https://doi.pangaea.de/10.1594/PANGAEA.940018 (accessed on 3 October 2024).
23. Graßl, S. Properties of Arctic Aerosols based on Photometer Long-Term Measurements in Ny-Ålesund. Ph.D. Thesis, Ludwig-Maximilians-Universität, München, Germany, 2019.
24. Graßl, S.; Ritter, C. Star Photometer Data (RAW) 2010–2021 from Ny-Ålesund, Svalbard (AWIPEV). 2021. Available online: https://doi.pangaea.de/10.1594/PANGAEA.937903 (accessed on 3 October 2024).
25. Inness, A.; Ades, M.; Agustí-Panareda, A.; Barré, J.; Benedictow, A.; Blechschmidt, A.M.; Dominguez, J.J.; Engelen, R.; Eskes, H.; Flemming, J.; et al. The CAMS reanalysis of atmospheric composition. *Atmos. Chem. Phys.* **2019**, *19*, 3515–3556. [CrossRef]
26. Smirnov, A.; Holben, B.; Eck, T.; Dubovik, O.; Slutsker, I. Cloud-screening and quality control algorithms for the AERONET database. *Remote Sens. Environ.* **2000**, *73*, 337–349. [CrossRef]
27. Li, J.; Carlson, B.E.; Lacis, A.A. How well do satellite AOD observations represent the spatial and temporal variability of PM2.5 concentration for the United States? *Atmos. Environ.* **2015**, *102*, 260–273. [CrossRef]
28. Wagner, J.; Ubele, A.A.; Schenzinger, V.; Kreuter, A. Extended Aerosol Optical Depth (AOD) time series analysis in an Alpine Valley: A Comparative Study from 2007 to 2023. *Aerosol Res. Discuss.* **2024**, *2*, 153–159. [CrossRef]
29. Xian, P.; Zhang, J.; O'Neill, N.T.; Reid, J.S.; Toth, T.D.; Sorenson, B.; Hyer, E.J.; Campbell, J.R.; Ranjbar, K. Arctic spring and summertime aerosol optical depth baseline from long-term observations and model reanalyses—Part 2: Statistics of extreme AOD events, and implications for the impact of regional biomass burning processes. *Atmos. Chem. Phys.* **2022**, *22*, 9949–9967. [CrossRef]
30. Tritscher, I.; Pitts, M.C.; Poole, L.R.; Alexander, S.P.; Cairo, F.; Chipperfield, M.P.; Grooß, J.U.; Höpfner, M.; Lambert, A.; Luo, B.; et al. Polar stratospheric clouds: Satellite observations, processes, and role in ozone depletion. *Rev. Geophys.* **2021**, *59*, e2020RG000702. [CrossRef]
31. von der Gathen, P.; Kivi, R.; Wohltmann, I.; Salawitch, R.J.; Rex, M. Climate change favours large seasonal loss of Arctic ozone. *Nat. Commun.* **2021**, *12*, 3886. [CrossRef]
32. Maturilli, M.; Neuber, R.; Massoli, P.; Cairo, F.; Adriani, A.; Moriconi, M.; Di Donfrancesco, G. Differences in Arctic and Antarctic PSC occurrence as observed by lidar in Ny-Ålesund (79 N, 12 E) and McMurdo (78 S, 167 E). *Atmos. Chem. Phys.* **2005**, *5*, 2081–2090. [CrossRef]
33. Massoli, P.; Maturilli, M.; Neuber, R. Climatology of Arctic polar stratospheric clouds as measured by lidar in Ny-Ålesund, Spitsbergen (79° N, 12° E). *J. Geophys. Res. Atmos.* **2006**, *111*, D09206. [CrossRef]
34. Hoffmann, A. Comparative Aerosol Studies Based on Multi-Wavelength Raman LIDAR at Ny-Ålesund, Spitsbergen. Ph.D. Thesis, Universität Potsdam, Potsdam, Germany, 2011.
35. Herrmann, R.; Ritter, C.; Böckmann, C.; Graßl, S. Improved Method for the Retrieval of Extinction Coefficient Profile by Regularization Techniques. *Remote Sens.* 2024, *in press*.

36. Ångström, A. On the Atmospheric Transmission of Sun Radiation and on Dust in the Air. *Geogr. Ann.* **1929**, *11*, 156–166. [CrossRef]
37. Gogoi, M.M.; Pandey, S.K.; Arun, B.; Nair, V.S.; Thakur, R.C.; Chaubey, J.P.; Tiwari, A.; Manoj, M.; Kompalli, S.K.; Vaishya, A.; et al. Long-term changes in aerosol radiative properties over Ny-Ålesund: Results from Indian scientific expeditions to the Arctic. *Polar Sci.* **2021**, *30*, 100700. [CrossRef]
38. Dada, L.; Angot, H.; Beck, I.; Baccarini, A.; Quéléver, L.L.; Boyer, M.; Laurila, T.; Brasseur, Z.; Jozef, G.; de Boer, G.; et al. A central arctic extreme aerosol event triggered by a warm air-mass intrusion. *Nat. Commun.* **2022**, *13*, 5290. [CrossRef]
39. Ansmann, A.; Ohneiser, K.; Engelmann, R.; Radenz, M.; Griesche, H.; Hofer, J.; Althausen, D.; Creamean, J.M.; Boyer, M.C.; Knopf, D.A.; et al. Annual cycle of aerosol properties over the central Arctic during MOSAiC 2019–2020–light-extinction, CCN, and INP levels from the boundary layer to the tropopause. *Atmos. Chem. Phys.* **2023**, *23*, 12821–12849. [CrossRef]
40. Grosfeld, K.; Treffeisen, R.; Asseng, J.; Bartsch, A.; Bräuer, B.; Fritzsch, B.; Gerdes, R.; Hendricks, S.; Hiller, W.; Heygster, G.; et al. Online sea-ice knowledge and data platform www.meereisportal.de. *Polarforschung* **2016**, *85*, 143–155. [CrossRef]
41. Maturilli, M.; Kayser, M. Homogenized Radiosonde Record at Station Ny-Ålesund, Spitsbergen, 1993–2014. 2016. Available online: https://doi.pangaea.de/10.1594/PANGAEA.845373 (accessed on 3 October 2024).
42. Maturilli, M. High Resolution Radiosonde Measurements from Station Ny-Ålesund (2017-04 et seq). 2020. Available online: https://doi.pangaea.de/10.1594/PANGAEA.914973 (accessed on 3 October 2024).
43. Graßl, S.; Ritter, C.; Schulz, A. The Nature of the Ny-Ålesund Wind Field Analysed by High-Resolution Windlidar Data. *Remote Sens.* **2022**, *14*, 3771. [CrossRef]
44. Ansmann, A.; Baars, H.; Chudnovsky, A.; Mattis, I.; Veselovskii, I.; Haarig, M.; Seifert, P.; Engelmann, R.; Wandinger, U. Extreme levels of Canadian wildfire smoke in the stratosphere over central Europe on 21–22 August 2017. *Atmos. Chem. Phys.* **2018**, *18*, 11831–11845. [CrossRef]
45. González, R.; Toledano, C.; Román, R.; Mateos, D.; Asmi, E.; Rodríguez, E.; Lau, I.C.; Ferrara, J.; D'Elia, R.; Antuña-Sánchez, J.C.; et al. Characterization of stratospheric smoke particles over the Antarctica by remote sensing instruments. *Remote Sens.* **2020**, *12*, 3769. [CrossRef]
46. Ohneiser, K.; Ansmann, A.; Chudnovsky, A.; Engelmann, R.; Ritter, C.; Veselovskii, I.; Baars, H.; Gebauer, H.; Griesche, H.; Radenz, M.; et al. The unexpected smoke layer in the High Arctic winter stratosphere during MOSAiC 2019–2020. *Atmos. Chem. Phys.* **2021**, *21*, 15783–15808. [CrossRef]
47. Tunved, P.; Ström, J.; Krejci, R. Arctic aerosol life cycle: Linking aerosol size distributions observed between 2000 and 2010 with air mass transport and precipitation at Zeppelin station, Ny-Ålesund, Svalbard. *Atmos. Chem. Phys.* **2013**, *13*, 3643–3660. [CrossRef]
48. Garrett, T.J.; Brattström, S.; Sharma, S.; Worthy, D.E.; Novelli, P. The role of scavenging in the seasonal transport of black carbon and sulfate to the Arctic. *Geophys. Res. Lett.* **2011**, *38*, L16805. [CrossRef]
49. Garrett, T.; Zhao, C.; Novelli, P. Assessing the relative contributions of transport efficiency and scavenging to seasonal variability in Arctic aerosol. *Tellus B Chem. Phys. Meteorol.* **2010**, *62*, 190–196. [CrossRef]
50. Eckhardt, S.; Stohl, A.; Beirle, S.; Spichtinger, N.; James, P.; Forster, C.; Junker, C.; Wagner, T.; Platt, U.; Jennings, S. The North Atlantic Oscillation controls air pollution transport to the Arctic. *Atmos. Chem. Phys.* **2003**, *3*, 1769–1778. [CrossRef]
51. Rinke, A.; Maturilli, M.; Graham, R.M.; Matthes, H.; Handorf, D.; Cohen, L.; Hudson, S.R.; Moore, J.C. Extreme cyclone events in the Arctic: Wintertime variability and trends. *Environ. Res. Lett.* **2017**, *12*, 094006. [CrossRef]
52. You, C.; Tjernström, M.; Devasthale, A.; Steinfeld, D. The role of atmospheric blocking in regulating arctic warming. *Geophys. Res. Lett.* **2022**, *49*, e2022GL097899. [CrossRef]
53. Yao, W.; Gui, K.; Zheng, Y.; Li, L.; Wang, Y.; Che, H.; Zhang, X. Seasonal cycles and long-term trends of arctic tropospheric aerosols based on CALIPSO lidar observations. *Environ. Res.* **2023**, *216*, 114613. [CrossRef] [PubMed]
54. Omar, A.H.; Winker, D.M.; Vaughan, M.A.; Hu, Y.; Trepte, C.R.; Ferrare, R.A.; Lee, K.P.; Hostetler, C.A.; Kittaka, C.; Rogers, R.R.; et al. The CALIPSO automated aerosol classification and lidar ratio selection algorithm. *J. Atmos. Ocean. Technol.* **2009**, *26*, 1994–2014. [CrossRef]
55. Ivănescu, L.; Baibakov, K.; O'Neill, N.T.; Blanchet, J.P.; Schulz, K.H. Accuracy in starphotometry. *Atmos. Meas. Tech.* **2021**, *14*, 6561–6599. [CrossRef]